






Pressure effects on mixing and combustion mode of a hydrogen/helium jet in cross-flow

Aanantha B. Murugavel¹ , James C. Massey^{1,2}  and Nedunchezian Swaminathan¹ 

¹Department of Engineering, University of Cambridge, Trumpington Street, Cambridge CB2 1PZ, UK

²Robinson College, University of Cambridge, Grange Road, Cambridge CB3 9AN, UK

Corresponding author: Anantha B. Murugavel, abm62@cam.ac.uk

(Received 5 December 2024; revised 23 May 2025; accepted 27 June 2025)

The pressure effects on the mixing fields of non-reacting and reacting jets in cross-flow are studied using large eddy simulation (LES). A hydrogen jet diluted with 30 % helium is injected perpendicularly into a cross-stream of air at four different pressures: 1, 4, 7 and 15 bar. The resulting interaction and the mixing fields under non-reacting and reacting conditions are simulated using LES. The subgrid scale combustion is modelled using a revised flamelet model for the partially premixed combustion. Good agreement of computed and measured velocity fields for reacting and non-reacting conditions is observed. Under non-reacting conditions, the mixing field shows no sensitivity to the pressure, whereas notable changes are observed for reacting conditions. The lifted flame at 1 bar moves upstream and attaches to the nozzle as the pressure is increased to 4 bar and remains so for the other elevated pressures because of the increasing burning mass flux with pressure. This attached flame suppresses the fuel–air mixing in the near-nozzle region. The premixed and non-premixed contributions to the overall heat release in the partially premixed combustion are analysed. The non-premixed contribution is generally low and occurs in the near-field region of the fuel jet through fuel-rich mixtures in the shear layer regions, and decreases substantially further with the increase in pressure. Hence, the predominant contributions are observed to come from premixed modes and these contributions increase with pressure.

Key words: turbulent mixing, computational methods, turbulent reacting flows

1. Introduction

The jet in cross-flow (JICF) is a canonical configuration widely recognised for its ability to enhance near-field fuel–air mixing and combustion characteristics, thereby finding

its use in various engineering applications (Margason 1993; Karagozian 2010; Mahesh 2013), such as gas turbine engines, where rapid fuel–air mixing is required to ensure safe combustion with minimal pollutant emissions. This requirement becomes even more critical when using highly reactive fuels such as hydrogen, which is coming up to achieve decarbonisation goals. Lean-premixed and lean direct injection (LDI) are current hydrogen injection strategies. In fully premixed combustion, fuel and air are homogeneously mixed before entering the combustion zone, facilitating ultra-low NO_x emissions, but this increases the risk of flame flashback leading to safety issues (Lieuwen *et al.* 2006). The LDI strategy reduces this risk by injecting fuel and air through separate streams, which produces partially premixed fuel–air mixtures in the combustion region. Despite this, LDI encounters flame anchoring challenges (York, Ziminsky & Yilmaz 2013) and is also prone to thermoacoustic oscillations, a common issue for many swirl-stabilised flame configurations. The JICF, conceptually similar to LDI, offers enhanced near-field mixing that promotes partial premixing of fuel and air. Additionally, a recirculation zone on the leeward side of the jet aids flame anchoring.

The jet and channel flows are relatively simple to investigate individually. However, the interaction between these two flows in JICF configuration generates complex vortical structures, as shown schematically in figure 1. The jet issuing in the z direction is introduced into a cross-flow along the x direction and this convention is followed throughout this study. The key parameters relevant for this flow are the jet-to-cross-flow density ratio, $S = \rho_j / \rho_{cf}$, velocity ratio, $R = U_j / U_{cf}$, and the momentum flux ratio, $J = \sqrt{SR^2}$. Here, the subscript j denotes the jet exit while cf refers to the cross-flow inlet. Additionally, the jet exit Reynolds number, $Re_j = U_j D / \nu_j$, where D is the jet exit diameter and ν is the kinematic viscosity of the jet fluid, and the cross-flow Reynolds number are also relevant parameters.

The prominent structure of a non-reacting JICF is the counter-rotating vortex pair (CVP), which is known to be the primary structure responsible for enhanced mixing of jet and cross-flow fluids. The formation and evolution of CVP influences these mixing attributes (Kamotani & Greber 1972; Moussa, Trischka & Eskinazi 1977; Broadwell & Breidenthal 1984; Smith & Mungal 1998). The formation of the CVP originates from the Kelvin–Helmholtz instability of the windward shear layer. Due to the pressure difference across the jet, the shear layer roll-up tilts and folds, gradually forming the CVP (Moussa *et al.* 1977; Muppidi & Mahesh 2005). Its spatial and temporal evolutions depend on the key parameters noted previously. Also, the cross-section of an equi-density JICF is observed to be distorted asymmetrically about the channel mid-plane (x – z plane in figure 1) when J is larger than 3.16 with $Re_j \approx 1900$ (Kuzo 1996; Smith & Mungal 1998; Getsinger *et al.* 2014). Further to the CVP, two other prominent unsteady structures are the horseshoe and wake vortices. The horseshoe vortices originate upstream of the jet exit and encircle the jet column. The wake vortices typically emanate from the boundary layer on the leeward side of the jet, drawing fluid from the boundary layer and entraining it into the jet plume. The characteristics of these structures also depend on the above mentioned key parameters (Fric & Roshko 1994; Kelso & Smits 1995; Smith & Mungal 1998). The dynamics of these structures contributes to the mixing of jet and cross-flow fluids, while some play a more significant role than others.

The characteristics of this mixing under non-reacting conditions have been quantified through numerous metrics in past studies. Smith & Mungal (1998) and Su & Mungal (2004) showed a rapid decrease of the jet fluid concentration along the jet centreline by studying the scalar concentration variations. Fearn & Weston (1974) also observed a similar decay for the centreline velocity, highlighting a correlation between the jet

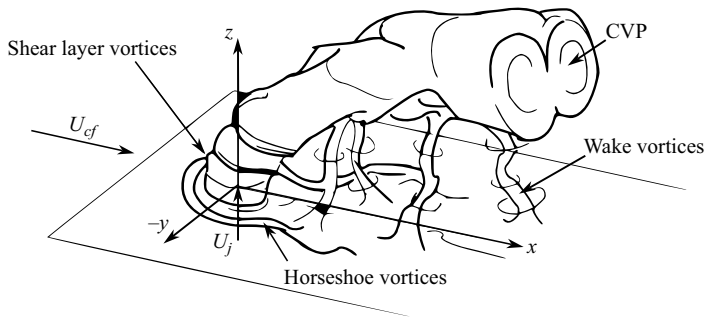


Figure 1. Schematics of the vortical structures in a jet in cross-flow, adapted from the study by Fric & Roshko (1994).

fluid concentration and its velocity. Following Smith & Mungal (1998), Hasselbrink & Mungal (2001) defined three regions of the flow: potential core, near-field and far-field, and identified a scaling law for the concentration decay in both the near- and far-field regions. Both Broadwell & Breidenthal (1984) and Hasselbrink & Mungal (2001) showed that the concentration decayed as s^{-1} in the near-field, which changed to $s^{-2/3}$ in the far-field region, where ' s ' is the distance along the jet centreline. However, Su & Mungal (2004) showed that such changes were not observed for a jet injected through a straight pipe with $J = 5.98$. These studies suggested that the mixing rate in JICF does not differ significantly from that of a free jet, showing a rate of s^{-1} . However, Smith & Mungal (1998) showed that the decay follows $s^{-1.3}$ for an equi-density jet ($S = 1$) issued from a converging nozzle with $10 \leq J \leq 25$.

The chemical reactions typically occur along the shear layer, where the jet fuel mixes with air in the cross-flow. The heat release resulting from these reactions suppresses the entrainment of surrounding (cross-flow) fluid (Hermanson & Dimotakis 1989), affecting the shear layer roll-up and its growth (Nair *et al.* 2019; Saini *et al.* 2021). Also, the heat release reduces the dominant frequency of this roll-up (Sayadi & Schmid 2021). These effects reduce the local mixing rate and thereby increase the jet penetration depth (Hasselbrink & Mungal 2001). The local mixing depends on the flame position since the heat release influences the entrainment and shear layer roll-up. Hence, there is a strong mutual dependence between these two physical processes, especially in flow configurations like JICF with highly unsteady large-scale flow dynamics. The majority of these studies are for atmospheric conditions.

Typically, industrial gas turbines operate at 15–30 bar with a combustor inlet air temperature of approximately 700 K and a turbine inlet temperature of 1800–2000 K (Rahman *et al.* 2011). Operating laboratory-scale burners under these conditions is challenging from safety and cost perspectives. In addition, the gases become relatively opaque for laser diagnostics at such high pressures, hence, high-fidelity measurements are quite challenging. For these reasons, typically preheated air at atmospheric pressure is used for experiments, which dictate the thermo-physical conditions for the simulations. Boxx *et al.* (2022) studied the reacting hydrogen jet flames at 7 bar with a primary focus on the stabilisation mechanism of the leeward flame branch. Using an identical configuration, Saini *et al.* (2020) studied the hydrogen enriched methane jet flames at 10 and 15 bar conditions and showed that neither the time-averaged nor the fluctuations of the velocity components are significantly altered by the change in pressure. However, the pressure effects on the overall mixing in the JICF remain unclear. Moreover, there is a strong mutual dependence between the local mixing and combustion characteristics, which is also not

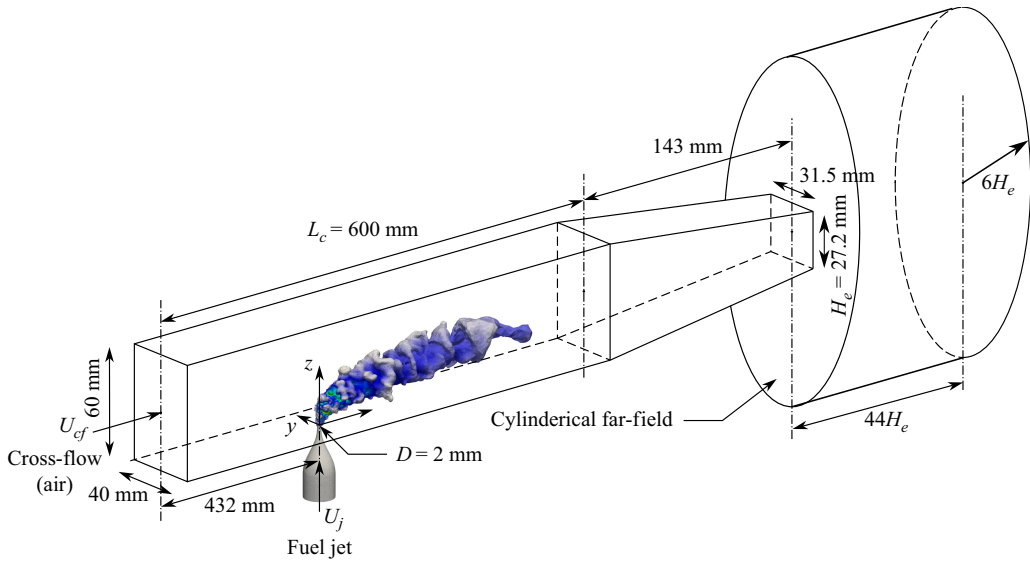


Figure 2. Geometry of the JICF configuration used for this study. The mixture fraction iso-surface, coloured by mean mixture fraction, shown is from one of the simulations studied to mark the relative position of the mixing region.

explored. Hence, this work aims to address these by conducting large eddy simulation (LES) of reacting hydrogen JICF investigated experimentally by Boxx *et al.* (2022). The specific objectives are to:

- (i) study the influences of pressure on the fuel–air mixing in non-reacting JICF, as a first step;
- (ii) study the combustion characteristics and their effects on the local mixing attributes;
- (iii) examine the pressure effects on the combustion and mixing attributes, and their mutual dependencies;
- (iv) investigate the changes in contributions of premixed and non-premixed modes with pressure to the overall heat release rate from the partially premixed combustion in the JICF.

The JICF configuration, flow conditions, modelling framework and the computational set-up are described in § 2. The validation of this computational model is discussed first in § 3, followed by the results on pressure effects on the mixing and combustion characteristics. The conclusions are summarised in § 4.

2. Flow condition and large eddy simulation

2.1. Experimental configuration

The JICF investigated experimentally by Boxx *et al.* (2022) is shown in figure 2. The preheated air at a temperature of $T_{cf} = 449$ K flows through a 600 mm long rectangular cross-flow duct with a cross-section of 40 mm \times 60 mm. A turning module with a converging nozzle is used to choke the cross-flow in the experiment so that a required operating pressure, p_0 , can be obtained in the duct. The effect of this module is represented using the cylindrical far-field domain and the required pressure is achieved by specifying p_0 for the simulation. The jet fuel has 70 % H_2 and 30 % He, and is preheated to a

Case	p_0 (bar)	\dot{Q}_T (kW)	\dot{m}_j (kg s ⁻¹)	\dot{m}_{cf} (kg s ⁻¹)	Re_j	Re_{cf}	$s_{L,st}$ (m s ⁻¹)	δ_{th} (μm)
P1	1	3	4.61×10^{-5}	0.016	2400	13 350	3.0	441.4
P4	4	11.8	1.82×10^{-4}	0.064	9600	51 200	2.88	78.6
P7	7	20.7	3.18×10^{-4}	0.110	16 800	92 000	2.64	41.0
P15	15	44.4	6.82×10^{-4}	0.240	36 000	1 92 000	2.13	18.3

Table 1. Cases investigated.

temperature of $T_j = 293$ K and injected as shown in figure 2. This nozzle has an exit diameter of 2 mm and is flush-mounted on the duct's bottom wall with its centre positioned at 432 mm from the cross-flow inlet as illustrated in the figure. The fuel mass flow rate is set to give a bulk mean velocity of 135 m s^{-1} at the nozzle exit. The air mass flow rate is set to give a bulk mean velocity of 8.89 m s^{-1} at the duct inlet with a centreline velocity of 10 m s^{-1} (described fully in § 2.3). These conditions are for the P7 case listed in table 1, which has $R = 15.8$, $S = 0.14$ and $J = 5.9$. Based on the reactants' composition at the inlets, the global equivalence ratio is $\phi_g = 0.05$, which gives a thermal power of $\dot{Q}_T = 20.7$ kW for the P7 case.

The flow conditions of the other three cases with 1, 4 and 15 bar investigated in this study are also listed in table 1. While the cross-flow is preheated, the thermochemical conditions are chosen such that the chemical reactions occur outside the explosion limit for all cases (von Elbe 1942). The velocity ratio R is kept to be the same for these four cases by changing the mass flow rates of the fuel jet and cross-flow, which changes \dot{Q}_T and the Reynolds numbers, as listed in table 1. However, S is kept constant, hence, J is the same for these four cases. The global equivalence ratio, ϕ_g , is the same for these cases since the fuel composition is the same. The lean, ξ_l , and rich, ξ_r , flammability limits, and the stoichiometric mixture fraction, ξ_{st} , are 0.017, 0.27 and 0.0513, respectively, for all the cases. Here, the flammability limits are defined such that the laminar flame speed is less than 5 % of the stoichiometric value outside this limit. The stoichiometric laminar flame speed, $s_{L,st}$, and its thermal thickness, δ_{th} , are also listed in table 1 for the four cases since these values change with pressure.

2.2. Modelling framework

The Favre-filtered mass, momentum and energy conservation equations are solved in the LES framework along with transport equations and closure models required for combustion. The mass and momentum equations are written respectively as

$$\frac{\partial \bar{\rho}}{\partial t} + \frac{\partial \bar{\rho} \tilde{u}_i}{\partial x_i} = 0, \quad (2.1)$$

$$\frac{\partial \bar{\rho} \tilde{u}_i}{\partial t} + \frac{\partial \bar{\rho} \tilde{u}_i \tilde{u}_j}{\partial x_j} = - \frac{\partial \bar{p}}{\partial x_i} + \frac{\partial \bar{\tau}_{ij}}{\partial x_j} - \frac{\partial \tau_{ij}^r}{\partial x_j}. \quad (2.2)$$

Here, the over-bar and $\tilde{}$ represent the filtered and Favre-filtered quantities, respectively, ρ is the density of the local mixture with velocity u_i in direction i , p is the pressure, and τ_{ij} is the molecular viscous stress tensor. The residual stress tensor at the subgrid level is $\tau_{ij}^r = \overline{\rho u_i u_j} - \bar{\rho} \tilde{u}_i \tilde{u}_j$, which is closed using the dynamic Smagorinsky model (Lilly 1992). The thermochemical state of the local mixture is obtained by solving the Favre-filtered transport equation of the enthalpy, h , mixture fraction, ξ , a reaction progress variable, c , and the two subgrid scale variances, $\sigma_{c,sgs}^2$ and $\sigma_{\xi,sgs}^2$. The mixture fraction is

defined following Bilger (1989) and the reaction progress variable is defined using the mass fraction of H_2O as $c = Y_{\text{H}_2\text{O}}/Y_{\text{H}_2\text{O}}^b$, where the superscript 'b' refers to the fully burnt mixture value which depends on the local mixture fraction, ξ . The Lewis numbers of all species used in the definition of c and ξ are close to unity.

The transport equations for key scalars can be written in a general form as (Chen, Ruan & Swaminathan 2017)

$$\frac{\partial \bar{\rho} \tilde{\varphi}}{\partial t} + \frac{\partial \bar{\rho} \tilde{u}_j \tilde{\varphi}}{\partial x_j} = \frac{\partial}{\partial x_j} \left(\bar{\rho} \mathcal{D}_{eff} \frac{\partial \tilde{\varphi}}{\partial x_j} \right) + \bar{S}_{\varphi}^+ - \bar{S}_{\varphi}^-, \quad (2.3)$$

where $\tilde{\varphi} = \{\tilde{h}, \tilde{c}, \sigma_{c,sgs}^2, \tilde{\xi}, \sigma_{\xi,sgs}^2\}$. The effective diffusivity is evaluated as $\mathcal{D}_{eff} = \mathcal{D}_{\varphi} + \nu_T/Sc_T$, where $Sc_T = 0.7$ and ν_T is the eddy viscosity. The molecular thermal diffusivity, α , is used for \mathcal{D}_{φ} in the transport equation of \tilde{h} and $\mathcal{D}_{\varphi} = \nu/Sc$ is used for other scalars with ν being the kinematic viscosity of the local mixture. A constant value of 0.7 is used for the Schmidt number, Sc , following previous studies (Ruan *et al.* 2012; Chen *et al.* 2020; Massey *et al.* 2023a). The source, \bar{S}_{φ}^+ , and sink, \bar{S}_{φ}^- , in (2.3) are

$$\bar{S}_{\varphi}^+ = \left\{ 0, \bar{\omega}^*, 2\bar{\rho} \frac{\nu_T}{Sc_T} |\nabla \tilde{c}|^2 + 2(\bar{c}\bar{\omega}^* - \tilde{c}\tilde{\omega}^*), 0, 2\bar{\rho} \frac{\nu_T}{Sc_T} |\nabla \tilde{\xi}|^2 \right\} \quad (2.4a)$$

$$\text{and } \bar{S}_{\varphi}^- = \left\{ 0, 0, 2\bar{\rho} \chi_{c,sgs}, 0, 2\bar{\rho} \chi_{\xi,sgs} \right\}. \quad (2.4b)$$

The source terms $\bar{\omega}^*$ and $\bar{c}\bar{\omega}^*$, and the subgrid scalar dissipation rates $\chi_{c,sgs}$ and $\chi_{\xi,sgs}$ require closure. The filtered reaction rate can be written as $\bar{\omega}^* = \bar{\omega}_{fp} + \bar{\omega}_{np}$, where the fully premixed and non-premixed contributions are

$$\bar{\omega}_{fp} = \bar{\rho} \int_0^1 \int_0^1 \frac{\dot{\omega}(\zeta, \eta)}{\rho(\zeta, \eta)} \tilde{P}(\zeta, \eta) d\zeta d\eta \quad (2.5a)$$

$$\text{and } \bar{\omega}_{np} = \bar{\rho} \tilde{c} \left(\frac{\nu}{Sc} |\nabla \tilde{\xi}|^2 + \chi_{\xi,sgs} \right) \int_0^1 \frac{1}{Y_{\text{H}_2\text{O}}^b} \frac{d^2 Y_{\text{H}_2\text{O}}^b}{d\eta^2} \tilde{P}(\eta) d\eta. \quad (2.5b)$$

The sample space variables for c and ξ are ζ and η , respectively. The joint Favre-filtered probability density function is approximated by two separate marginal β functions; one for c and another one for ξ . The $\bar{c}\bar{\omega}^*$ is evaluated in a similar manner to $\bar{\omega}_{fp}$. The SGS scalar dissipation rate $\chi_{c,sgs}$ is closed using an algebraic model proposed by Dunstan *et al.* (2013) and $\chi_{\xi,sgs}$ is closed using the linear relaxation model with a model constant of 2 (Janicka & Peters 1982; Pierce & Moin 1998). The past studies have established that the parameters of the algebraic model employed for $\chi_{c,sgs}$ are closely connected with certain aspects of turbulence, combustion and their mutual interactions, and hence they are not tuneable. The parameter β_c represents the influence of curvature induced by flame wrinkling (Kolla *et al.* 2009; Dunstan *et al.* 2013; Langella & Swaminathan 2016; Langella *et al.* 2016a,b; Chen *et al.* 2017; Massey, Langella & Swaminathan 2018; Chen *et al.* 2019; Massey *et al.* 2023a). Murugavel *et al.* (2024) considered $\beta_c = 4$ and 7.5 to show that the JICF results are almost insensitive to this parameter value and hence, the commonly used value of 7.5 is adopted for this study.

The Favre-filtered temperature, \tilde{T} , is obtained using the computed \tilde{h} since $\tilde{c}_p(\tilde{T} - T_0) = (\tilde{h} - \Delta h_f^0)$. Here, c_p , Δh_f^0 and T_0 are the mixture specific heat capacity, formation enthalpy and reference temperature, respectively. Both c_p and ν vary with the local temperature, and the mixture density is calculated using the state equation. The molecular

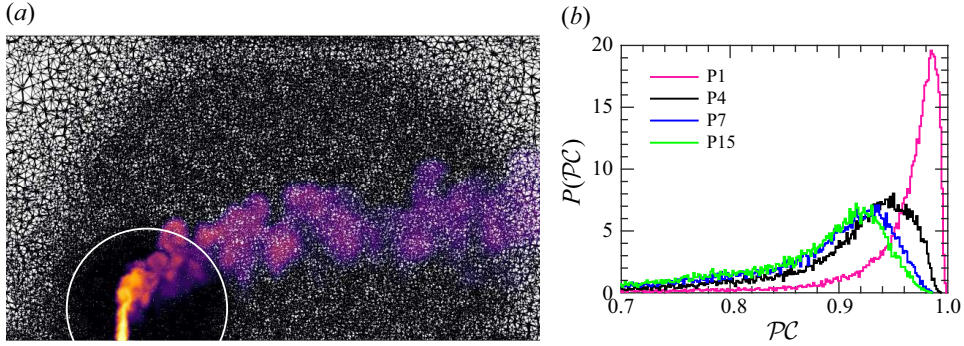


Figure 3. (a) Computational cells in the jet region and (b) the p.d.f. of Pope criterion, $P(PC)$, in this region.

mass required for the state equation, c_p , Δh_f^0 , ν and $\dot{\omega}(\zeta, \eta)$ are all pre-computed using premixed laminar flame calculations, as discussed by Massey *et al.* (2023b), which are undertaken using Cantera (Goodwin, Moffat & Speth 2017) with DLR-SyNG reaction mechanism (Methling, Braun-Unkhoff & Riedel 2020) and stored in a look-up table for use during LES. Soret and Dufour effects are neglected since the turbulent transport is expected to be dominant compared with these molecular fluxes in LES. Additionally, the variation of $\dot{\omega}(\zeta, \eta)$ and $d^2Y_{H_2O}^b/d\eta^2$ in ζ – η space does not depend on whether they are from premixed or non-premixed flamelets. The above mentioned modelling framework has been tested extensively for a variety of flow and flame configurations – premixed laboratory scale piloted Bunsen (Langella & Swaminathan 2016) and bluff body stabilised flames (Langella *et al.* 2016a, b; Massey *et al.* 2018), and partially premixed flames in gas turbine engines (Chen *et al.* 2019). The specifics of the validation can be found in those studies. Murugavel *et al.* (2024) has validated this modelling for atmospheric JICF, and further validation for a high-pressure, 7 bar, JICF is discussed later in §§ 3.1.1 and 3.2.1.

2.3. Computational set-up

The computational volume includes the cross-flow channel, jet nozzle and an additional cylindrical domain shown in figure 2. The additional domain is used to specify a set of clear exit boundary conditions. This volume is discretised using approximately 5.4 M unstructured tetrahedral cells with the finest grid resolution having an average grid size of approximately 0.15–0.4 mm in the near-nozzle region as shown in figure 3(a). The predominant mixing of the jet fuel with the cross-flowing air occurs in this region; hence, a fine grid is required. The ability of this grid to resolve the dynamic scales is assessed using the Pope criterion (PC), which is defined as the ratio of resolved to the total (resolved + subgrid) kinetic energies (Pope 2000). Under the isotropic turbulence assumption, the resolved kinetic energy is approximated as $\langle \tilde{k}_{res} \rangle = 0.5(\langle \sigma_{u_x, res}^2 \rangle + \langle \sigma_{u_y, res}^2 \rangle + \langle \sigma_{u_z, res}^2 \rangle)$, where the resolved variance of the velocity is computed as $\langle \sigma_{u_i, res}^2 \rangle = \langle \tilde{u}_i^2 \rangle - \langle \tilde{u}_i \rangle^2$. The angled brackets here and in the following discussions denote time averaging. The subgrid kinetic energy is estimated as $\tilde{k}_{sgs} \approx 3u_{\Delta}^2/2$, where the subgrid-scale velocity fluctuation is approximated using the eddy viscosity model as $u'_{\Delta} \approx C\nu_T/\Delta$ with C and Δ being the model constant and the local grid size, respectively. The probability density function (p.d.f.) of this criterion constructed using 500 bins for the samples taken within the regions marked using the white line in figure 3(a) clearly shows that more than 90 % of the kinetic

energy is captured by the grid, as demonstrated in [figure 3\(b\)](#). As the Reynolds number increases with pressure, the kinetic energies of the small-scale structures also increase. Therefore, the kinetic energy being resolved by the grid decreases. However, the figure shows that the grid resolves more than 80 % of the kinetic energy over the range of pressure conditions investigated in this study. The suitability of the grid and the modelling framework to capture statistics of flow and flame attributes in the JICF is examined further in §§ [3.1.1](#) and [3.2.1](#).

A well-developed channel flow is obtained by performing an LES of a 1 m long channel with a cross-section of 40 mm × 60 mm. The mass flow rate was set to give a uniform velocity profile of 8.89 ms⁻¹ at this channel inlet. The fully developed profile from the channel's exit plane was then imposed as the cross-flow inlet boundary condition in the JICF domain. In addition, the streamwise integral length scales and Reynolds stress tensor from the channel's exit plane are used to define the JICF inlet turbulence using the synthetic eddy model of Jarrin *et al.* (2006). The CFD implementation of this eddy model is explained by Chen *et al.* (2020). The mass flow rate of the jet is prescribed at the inlet of the converging nozzle with no turbulence. A wave transmissive boundary condition is specified for the domain outlet to prevent acoustic reflection. The walls are specified to be no-slip with the Spalding wall function (Spalding 1961), which gives

$$y^+ = u^+ + \frac{1}{\hat{a}} \left[e^{\hat{b}u^+} - 1 - \hat{b}u^+ - \frac{1}{2}(\hat{b}u^+)^2 - \frac{1}{6}(\hat{b}u^+)^3 \right] \quad (2.6)$$

for the velocity variation across the boundary layer. Here, y^+ and u^+ are the dimensionless wall-normal distance and the velocity, respectively. The von Kármán and the empirical constant, denoted \hat{b} and \hat{a} , respectively, take the values 0.41 and 9.8.

The additional cylindrical domain walls are specified with a slip condition. All walls are specified to be adiabatic since no wall temperature was measured in the experiment. All scalar variables are set to have zero gradient at the computational outlet boundary with a prescribed pressure so that the cross-flow inlet pressure matches its measured value, p_0 . The simulations are run using OpenFOAM v7 code (Weller *et al.* 1998) with a PIMPLE algorithm. As strong density gradients are present under reacting conditions, this algorithm is modified with density coupling to include compressibility effects (rhoPimpleFoam solver), as schematically illustrated in figure 2 of Murugavel *et al.* (2024). A second-order central difference scheme is used for the spatial gradients, while an implicit Euler scheme is used for time marching. The simulations are run for approximately $12\tau_f$ in total, where τ_f is the flow-through time defined as L_c/U_{cf} (see [figure 2](#)). The non-reacting flow starting from a quiescence is allowed to evolve for approximately $6\tau_f$ with samples collected over the second $3\tau_f$ for calculating the cold-flow statistics. The first $3\tau_f$ are allowed for transients to escape the domain. The mixture is ignited at $6\tau_f$ and the ignition transients are allowed to escape before collecting samples over the final $3\tau_f$ of the total simulation duration of $12\tau_f$. Also, collecting samples over a longer period does not unduly alter the statistics discussed in this paper.

3. Results and discussion

3.1. Non-reacting jet in cross-flow

3.1.1. Validation

Boxx *et al.* (2022) used high-speed (10 kHz) stereoscopic particle image velocimetry (SPIV) for both non-reacting and reacting flows along with dual-plan laser-induced fluorescence of hydroxyl radical (OH-PLIF) to study flame attributes at 7 bar.

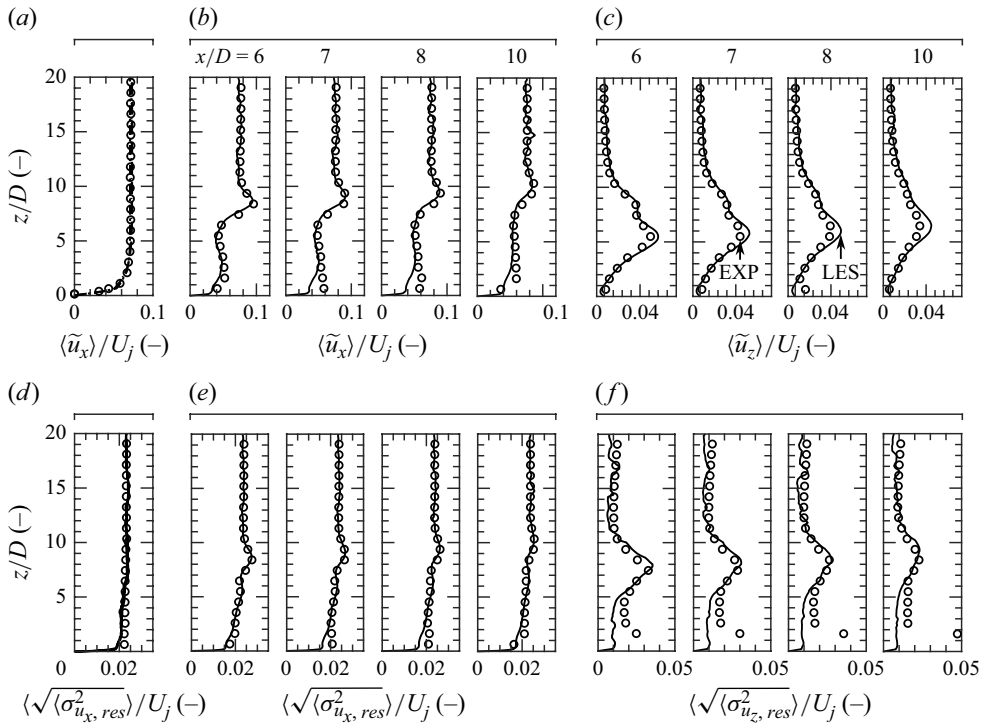


Figure 4. Comparisons of measured (\circ) and computed ($—$) (a,b) mean axial and (c) cross-stream velocities, and (d–f) their respective variances at four axial locations for the case P7-NR. The variations of $\langle \tilde{u}_x \rangle$ and $\sqrt{\langle \sigma_{u_x, res}^2 \rangle}$, both normalised by U_j , at several locations upstream of the jet are shown in panels (a) and (d).

The diagnostics details can be found from Boxx *et al.* (2022). Figure 4 compares the measured and computed mean value of \tilde{u}_x and \tilde{u}_z , along with their root-mean-square (r.m.s.) values, for the non-reacting flow at 7 bar. The r.m.s. values are computed using the resolved velocity variances as $\sqrt{\langle \sigma_{u_i, res}^2 \rangle}$. Figures 4(a) and 4(d) present the cross-stream variation of $\langle \tilde{u}_x \rangle$ and $\sqrt{\langle \sigma_{u_x, res}^2 \rangle}$, respectively, measured at 10 mm upstream of the jet exit ($x = -5D$). These are compared with LES results extracted at four axial positions: $x = -5D$, $-25D$, $-50D$ and $-100D$. The computed values at all four locations overlap since the cross-flow is fully developed, and also agree well with the measurements at $x = -5D$. Also, the presence of the jet is not felt at this x location. Streamlines plotted on the mid-axial and $z = 2D$ planes (not shown) suggest that the jet's influence is felt by the cross-flow, as indicated by the deflections of the streamlines, only after $x = -2.5D$. This upstream location does not change with pressure since J is kept constant for the four cases of table 1. The strong agreement in figures 4(a) and 4(d) demonstrates that the inflow velocities and turbulence characteristics of the cross-flow, which are obtained from a separate LES of the channel flow, are well matched with the experiment. Figures 4(b) and 4(c) compare the mean velocity components in the mixing region, while figures 4(e) and 4(f) present the corresponding r.m.s. values. The good agreement between simulation and experiment for both the mean and fluctuating components of velocity confirms the reliability of the numerical model for studying scalar mixing under the operating conditions of interest.

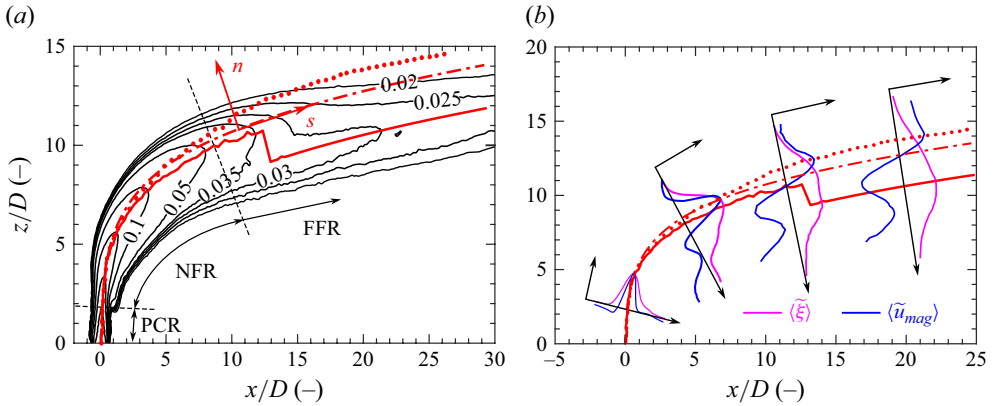


Figure 5. (a) Spatial distribution of $\langle \tilde{\xi} \rangle$ in the mid- y plane for the P1-NR case. (b) Corresponding radial variations of $\langle \tilde{u}_{mag} \rangle$ and $\langle \tilde{\xi} \rangle$ at some locations along the jet, within the same plane. Overlaid on these plots are the trajectories, defined as the locus of peak values of $\langle \tilde{u}_{mag} \rangle$ (.....) and $\langle \tilde{\xi} \rangle$ (—), and the streamline originating from the jet centre (— · —).

3.1.2. Jet trajectory and cross-sectional asymmetry

The spatial evolution of the jet centreline, called as jet trajectory, is of fundamental interest. This trajectory can be defined using the velocity or scalar concentration, though this choice can influence the results. The scalar-based definition is often preferred in studies focusing on mixing as it directly reflects the distribution and penetration of jet fluid into the cross-flow. For instance, Smith & Mungal (1998) defined the trajectory as the locus of maximum jet fluid concentration in the mid- y plane, where the local maximum is obtained from the radial distribution of the scalar as illustrated in figure 5(b). Figures 5(a) and 5(b) show this trajectory for the case P1-NR, identified using the time-averaged mixture fraction field, $\langle \tilde{\xi} \rangle$, where $\langle \tilde{\xi} \rangle = 1$ corresponds to pure jet fluid and $\langle \tilde{\xi} \rangle = 0$ to the cross-flow fluid. However, this trajectory exhibits discontinuity around $x/D \approx 12$, arising from the asymmetric distribution of the jet fluid about the $y = 0$ plane. As shown in the top row of figure 6 for the case P1-NR, the jet fluid is concentrated more in one (left) lobe of the CVP, which leads to the discontinuity in the trajectory. Due to this, the scalar-based trajectory is not used in this study. Alternative definitions have been proposed in the past: Fearn & Weston (1974) used the locus of maximum velocity magnitude, but Kamotani & Greber (1972) showed that velocity-based trajectories typically penetrate 5 %–10 % deeper than scalar-based ones, as seen in figure 5. The current study adopts the streamline-based trajectory used by Hasselbrink & Mungal (2001) to avoid the limitations of the other two methods. The trajectory is defined as the streamline originating from the jet exit centre. This approach avoids discontinuities from asymmetry and yields a trajectory that aligns more closely with scalar-based definitions (see figure 5), consistent with those reported by Yuan & Street (1998). A curvilinear orthogonal coordinate system (s - n - y) is then constructed using the streamline-based jet trajectory. As illustrated in figure 5(a), the s -axis follows this trajectory, with the distance along s computed as a piecewise integral along the streamline. The n -axis represents the local normal direction in the x - z plane, perpendicular to the trajectory, while the y -axis is along the lateral direction.

The distribution of $\langle \tilde{\xi} \rangle$ in different y - n planes along the jet trajectory is shown in figure 6, revealing an asymmetric distribution of the jet fluid about the mid- y plane for all the pressures listed in table 1. In the near-nozzle region, $s/D < 1.8$, the distribution is nearly symmetric, but this symmetry breaks in the region $1.8 < s/D < 20$, as observed

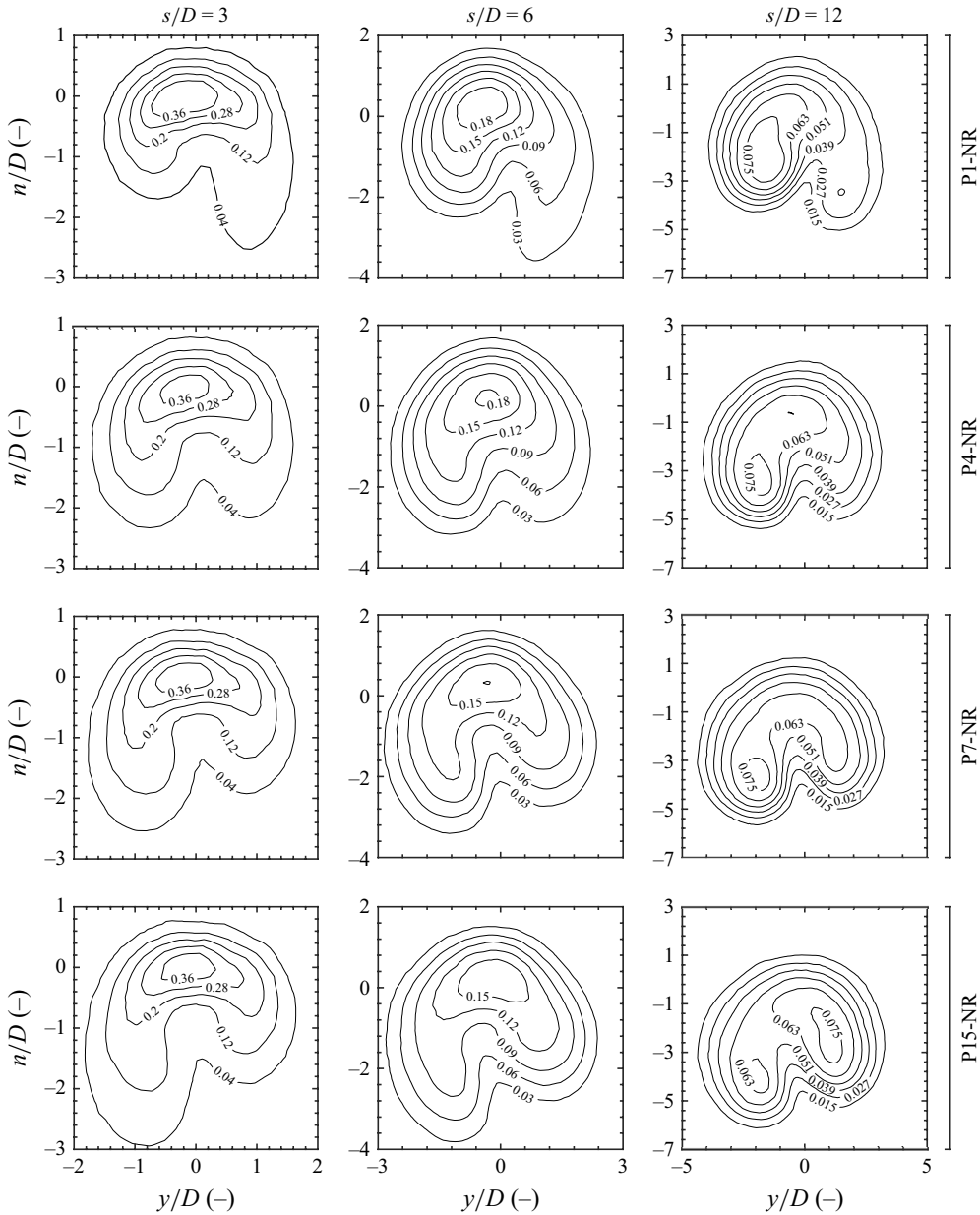


Figure 6. Spatial distribution of $\tilde{\xi}$ in the jet cross-section for three s/D locations.

from figure 5. Previous studies have reported similar observations. For equi-density jets with $R = 5, 10$ and 20 , Kuzo (1996) observed that asymmetry becomes more pronounced when Re_j falls below a particular value, which increases with R . Getsinger *et al.* (2014) noted that such asymmetry correlates with the shear layer instability in their experimental investigations. Specifically, jets issuing from a wall-mounted converging nozzle with $1800 \leq Re_j \leq 3000$ exhibited a transition in the shear layer behaviour – from absolutely unstable to convectively unstable – as J^2 was increased above 10 or S above 0.4 . In the present study, although $J^2 \approx 35$ places the jet in the convectively unstable regime,

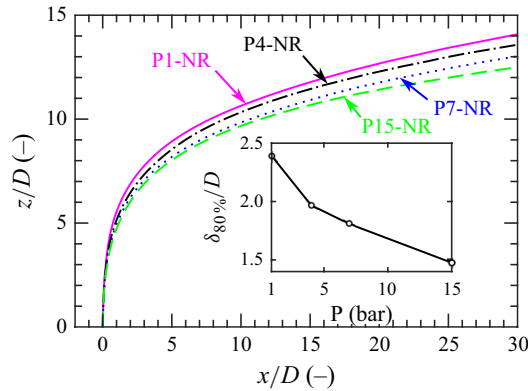


Figure 7. Influence of pressure on the jet trajectory based on the central streamline. The inset shows the variation of the cross-flow boundary layer thickness with pressure.

where asymmetries are expected, $S = 0.14$ remains well below the convective instability threshold suggested by Getsinger *et al.* (2014). It is also important to note that the Re_j in this study is significantly higher than those of Getsinger *et al.* (2014), except for case P1. Furthermore, a past DNS study of an equi-density JICF with $R = 6$ and $Re_j = 5000$ (Muldoon & Acharya 2010) suggested that asymmetry may also be influenced by boundary conditions.

The unstructured tetrahedral grid used in this study could, in principle, introduce asymmetries via the boundary conditions. However, an inspection of the spatial grid distribution reveals no asymmetry within the grid tolerance of $1 \mu\text{m}$. Uniform profiles are prescribed at the inlets for all scalar quantities and the velocity field shows no evidence of asymmetry. Moreover, the same grid and similar boundary conditions are employed across all simulations. Despite this consistent set-up, variations in the asymmetry of $\langle \xi \rangle$ are observed across cases, as seen in figure 6. In the P1-NR case, the jet fluid is concentrated on the $-y$ side (towards the reader) while at higher pressures, the concentration shifts towards the $+y$ side. This behaviour is particularly evident in the last column of figure 6. This shift suggests that neither the grid nor the boundary conditions are the likely sources of the symmetry-breaking phenomenon. Instead, the asymmetry is attributed to the convective instability characteristics of the shear layers, which are primarily governed by Re_j . As a result, the direction of asymmetry – whether towards the $+y$ or $-y$ side – is equally likely if the simulations are repeated.

The streamline-based trajectory is shown in figure 7 for the four cases. The jet penetration depth is higher in P1-NR and it decreases with increasing pressure. These differences arise from neither the grid nor the momentum flux ratio, since both of these are kept the same for these cases. Increasing the pressure from 1 to 15 bar increases the cross-flow Reynolds number by a factor of approximately 14.4. Consequently, the cross-flow boundary layer becomes thinner (see the inset of figure 7) and this layer is defined as the wall-normal distance where the cross-flow velocity reaches 80 % of the centreline value as suggested by Muppidi & Mahesh (2005). These boundary layer thicknesses are calculated for the four axial locations considered for figure 4(a), and this thickness at $x = -25D$ is shown in the inset of figure 7 for the four pressures. The Reynolds number for the cross-flow increases with p_0 , as listed in table 1, and hence the boundary layer becomes thinner. The thickness shown in the inset does not vary significantly with x since the cross-flow is observed to be fully developed as demonstrated in figure 4(a). The jet in the P1-NR case is issuing into a cross-flow with a thicker boundary layer, hence, it experiences relatively

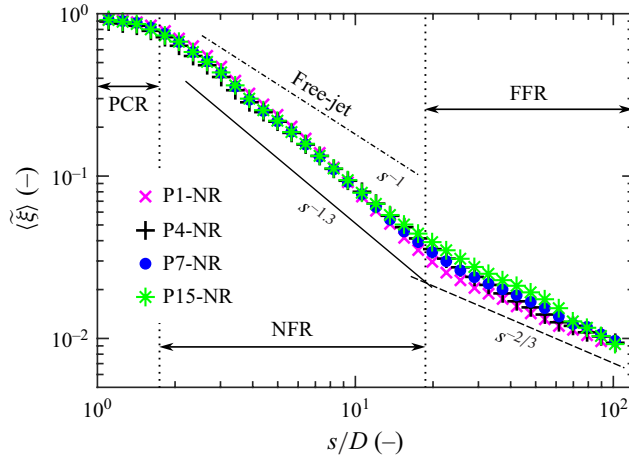


Figure 8. Variation of $\langle \tilde{\xi} \rangle$ with s/D for the four cases under non-reacting conditions.

lower cross-flow momentum in the near-nozzle region. Thus, it penetrates deeper into the cross-flow compared with those for the elevated pressures. This is similar to the behaviour observed by Muppidi & Mahesh (2005) in their DNS study of incompressible JICF at atmospheric pressure.

3.1.3. Mixing performance

The jet entrains and mixes with the surrounding fluid, leading to its spatial spread. This mixing is typically quantified using the centreline decay of $\langle \tilde{\xi} \rangle$ and unmixedness, $g_{\xi} = \langle \sigma_{\xi}^2 \rangle / \langle \tilde{\xi} \rangle (1 - \langle \tilde{\xi} \rangle)$, where σ_{ξ}^2 denotes the variance of the mixture fraction. The normalisation quantity is essentially the maximum variance obtained when the fluid is stirring but neither mixing nor diffusing (Dimotakis & Miller 1990). The total variance σ_{ξ}^2 is the sum of both the resolved and subgrid variances. The variation of $\langle \tilde{\xi} \rangle$ along s is often regarded as a reliable indicator of a jet's overall evolution due to entrainment and mixing, and thus it is commonly used to characterise mixing in the JICF configuration (Smith & Mungal 1998). This variation is shown in figure 8 for the four pressures along with several power-laws reported in previous studies (Broadwell & Breidenthal 1984; Smith & Mungal 1998; Hasselbrink & Mungal 2001; Su & Mungal 2004). The mixture fraction decreases monotonically with increasing s , following an initial region close to the jet exit. The initial portion of the jet, known as the potential core region (PCR), is marked in the figure. The PCR behaves similar to an axisymmetric mixing layer, where similarity solutions are generally not expected. Its length, s_0 , is the distance along s where $\langle \tilde{\xi} \rangle$ drops to 0.9. This length is approximately $1.8D$ and remains independent of pressure. Based on the entrainment vortex sheet model of Coelho & Hunt (1989), Hasselbrink & Mungal (2001) derived an analytical expression for s_0 . A leading-order approximation of the expression suggests that $s_0 \propto S^{1/2}/J$. Since S and J are held constant, s_0 remains unchanged for the conditions studied.

The flow in the near-field region (NFR) has often been described as similar to the fully developed regime of a free turbulent jet without significant deflection in the cross-flow direction. Accordingly, Hasselbrink & Mungal (2001) observed that the jets in this region follow a self-similar solution similar to that of free jets, where $\langle \tilde{\xi} \rangle$ decays as s^{-1} . However, this assumption typically holds for jets with $J \gg 10$. The present study has $J < 10$; hence, early jet deflection and the formation of the CVP lead to a deviation from the axisymmetric

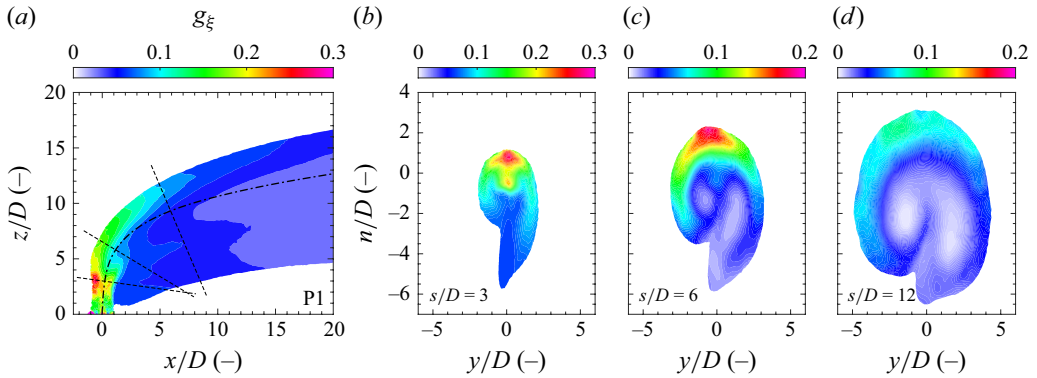


Figure 9. (a) Typical spatial variation of g_ξ in the $y = 0$ plane. The variation in y - n planes at locations marked in panel (a) are shown in panels (b–d). The distribution is shown here for the case P1-NR.

jet behaviour and accelerated decay of $\langle \tilde{\xi} \rangle$. As a result, a steeper decay of approximately $s^{-1.3}$ is observed, which is also independent of pressure for the reasons noted above. The NFR extends up to $s \approx 30D$ in the P1-NR case and up to $20D$ in the P15-NR case. Beyond this point lies the far-field region (FFR), where the jet has fully evolved into a coherent CVP translating with the cross-flow. As the jets reach their fully developed state, the entrainment diminishes, yielding a slower decay of $\langle \tilde{\xi} \rangle$ following $s^{-2/3}$ trend – again showing no significant dependence on pressure.

The centreline decay of the mixture fraction does not capture the full spatial distribution of jet fluid, specifically the asymmetric features observed in figure 6. Therefore, a global quantification of the degree of mixing is imperative. Although turbulence is responsible for stirring the jet and cross-flow fluids at large scales, it indirectly enhances mixing by increasing the mixture fraction gradient, $\nabla \xi$. It is also well known that this gradient is directly proportional to σ_ξ^2 and thereby proportional to g_ξ . It is important to note that g_ξ represents the degree of segregation between two fluids, rather than a direct measure of the mixing rate. Its spatial distribution highlights the regions of strong scalar gradients – a condition conducive to intense local mixing. In regions of spatially uniform $\langle \tilde{\xi} \rangle$, σ_ξ^2 and g_ξ are zero, whether the fluid is fully mixed or completely unmixed. The maximum value of $g_\xi = 1$ occurs in regions where the two fluids are in contact but remain unmixed. Intermediate values arise where the fluids are diffusing. Hence, g_ξ can be used for characterising local mixing. Figure 9 shows the spatial distribution of g_ξ for case P1-NR. Its distribution in the $y = 0$ plane, shown in figure 9(a), indicates that the highest value of g_ξ occurs in the near-nozzle region, peaking near the end of the PCR ($s/D \approx 1.8$), where the windward and leeward jet shear layers merge. This region corresponds to intense shear-driven roll-up and high scalar gradients, suggesting the potential for the most intense mixing. Beyond the PCR, g_ξ decreases with increasing s , indicating a reduction in fluid segregation and thereby the progression in mixing. However, large values of g_ξ persist in localised regions. For example, at $s/D = 3$ (see figure 9b), high mixture fraction gradients appear on both sides of the jet, producing two local maxima in g_ξ (at $n \simeq \pm D$). Further downstream, the influence of the leeward recirculation zone diminishes, and thus there is a single peak at $s/D = 6$. The strength of the local maxima reduces further by $s/D = 12$ due to upstream mixing. This pattern reflects how the entrainment of cross-flow fluid and the action of CVP stretch the jet laterally in the y -direction, distributing the jet fluid around the periphery of the CVP and expanding the area over which it is distributed. As a result,

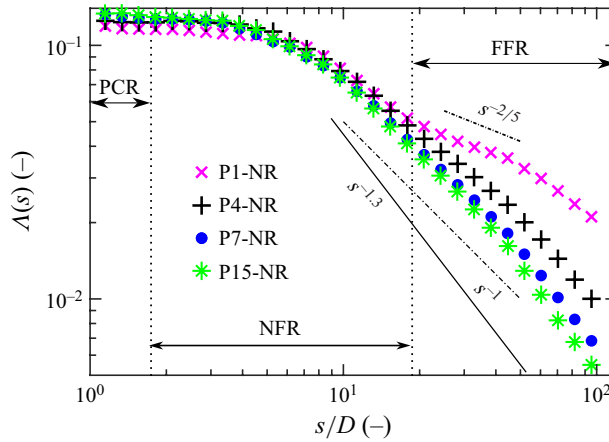


Figure 10. Variation of the integrated unmixedness, Λ , with s/D .

scalar gradients and local segregation level reduce. These spatial patterns are almost the same for all cases listed in [table 1](#).

For quantifying the rate at which the mixing progresses along the jet, another measure of unmixedness, Λ , can be defined as

$$\Lambda(s) = \frac{1}{A} \int_A g_{\xi} dA = \frac{1}{A} \int_A \frac{\langle \sigma_{\xi}^2 \rangle}{\langle \xi \rangle (1 - \langle \xi \rangle)} dA, \quad (3.1)$$

where A is the jet cross-sectional area in the y - n plane. The iso-contours of $\langle \xi \rangle = 0.003$, corresponding to the global mixture fraction, bound the area used for (3.1). Hence, the values corresponding to the pure oxidiser are excluded from the calculation. The quantity Λ represents the cross-sectionally averaged normalised mixture fraction variance. High values of Λ correspond to predominantly segregated mixtures, whereas low values indicate a well-mixed fluid. The variation of Λ along the jet trajectory is shown in [figure 10](#) for the four cases. The variation of Λ exhibits a trend similar to that of $\langle \xi \rangle$ (see [figure 8](#)). The fluids are largely segregated in the potential core region (PCR), resulting in high Λ values, which decrease along the jet due to turbulent and molecular mixing. Since Λ incorporates variance across the entire jet cross-section, including off-centre regions, the decay in the NFR begins slowly. Beyond $s/D \approx 7$, the decay follows an s^{-1} trend, which is slightly slower than the $s^{-1.3}$ decay observed for $\langle \xi \rangle$. While the decay of Λ in the NFR is observed to be less sensitive to p_0 , notable pressure dependence emerges in the FFR. As shown in [figure 10](#), the decay exponent magnitude decreases as p_0 is reduced, suggesting that mixing in the FFR improves with increasing pressure. It is important to note that Λ represents the variance normalised by $\langle \xi \rangle (1 - \langle \xi \rangle)$. The behaviour of the area-weighted mean mixture fraction, $\int_A \langle \xi \rangle dA / A$, exhibits a trend similar to that shown in [figure 8](#) with a far-field decay rate of approximately $s^{-2/3}$ that is largely independent of p_0 . This suggests that the decay of $\langle \xi \rangle (1 - \langle \xi \rangle)$ is also insensitive to p_0 in the FFR. Consequently, the observed sensitivity of Λ to p_0 emerges primarily from $\langle \sigma_{\xi}^2 \rangle$ variations. As discussed previously, mixing in the FFR is dominated by turbulence. Increasing p_0 raises the cross-flow Reynolds number, enhancing turbulent dissipation and accelerating the decay of scalar variance. These second-order statistics are more sensitive to turbulence effects than the mean mixture fraction. Although local mixing intensity varies slightly

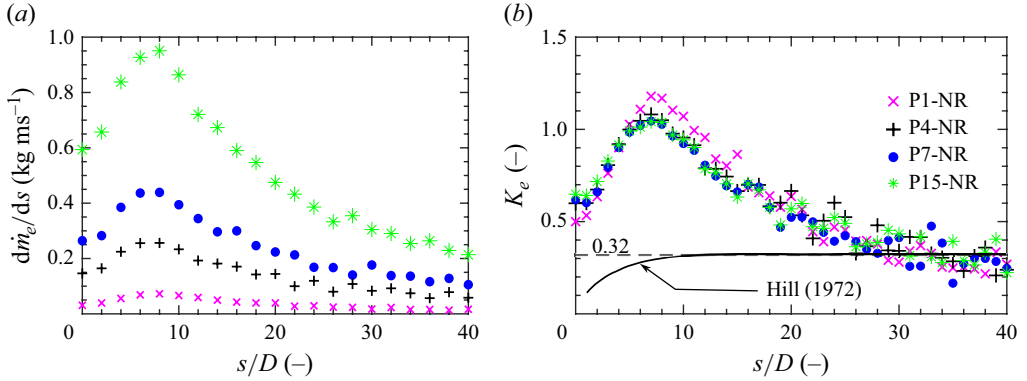


Figure 11. Variations of (a) \dot{m}_e/ds and (b) K_e with s/D .

across the cases, the overall trend of Λ remains largely unaffected. This indicates that the peak g_ξ near the end of the PCR and its gradual spreading in the downstream, as observed in figure 9, does not vary significantly with pressure.

3.1.4. Entrainment rate

Fundamentally, a jet entrains the surrounding fluid into its region of influence, causing the mass flow rate across this region to increase with distance along the jet trajectory, s . This entrained mass flow rate, \dot{m}_e , up to a location s , can be obtained through $\dot{m}_e = \dot{m}(s) - \dot{m}_j$, where $\dot{m}(s)$ and \dot{m}_j are the mass flux, $\rho u_i n_i$, integrated over the jet cross-section at location s and the jet exit, respectively. The variations of \dot{m}_e/ds obtained from the LES results are shown in figure 11(a) for the four cases. The entrainment rate varies along the jet due to a shift in the dominant entrainment mechanism. The Kelvin–Helmholtz instabilities cause the shear layers to roll up in the near-nozzle region, initiating the formation of the CVP. As shown by Nair *et al.* (2019), the swirling strength of these shear-layer vortices increases with s , which increases the entrainment rate, reaching a peak rate between $s/D = 6$ and 8. Further downstream, after the jet had bent and almost levelled off, the dominant mechanism transitions to turbulence generated by the jet itself since the fluid that has emerged from the jet travels in the same direction as the cross-flow. However, this turbulence is typically less energetic than the shear-layer-driven turbulence in the near-field, resulting in a lower entrainment rate (Kankanwadi & Buxton 2023). Additionally, the local rate of jet-to-cross-flow entrainment increases proportionally with pressure.

The entrainment rate of the jet in a co-flowing stream was studied extensively in the past, and the resulting scaling can be expressed as (Hill 1972)

$$\hat{m}_e = \frac{\dot{m}_e}{\dot{m}_j} = K_e \left(\frac{s}{D} \right) S^{-\frac{1}{2}}, \quad (3.2)$$

where s and S are respectively the axial distance from the jet exit and the density ratio defined earlier. The dimensionless number K_e is called the entrainment rate coefficient, which is the normalised rate of entrainment and is calculated as

$$K_e(s) = \frac{d\dot{m}_e}{ds} \left(\frac{D}{\dot{m}_j} \right) S^{\frac{1}{2}}. \quad (3.3)$$

The past measurements of jet in co-flow showed (Hill 1972) that K_e varied with s , as depicted in figure 11(b), and it plateaued to a constant value of 0.32 in the far-field region. In the JICF configuration studied here, the relatively large values of K_e , in the

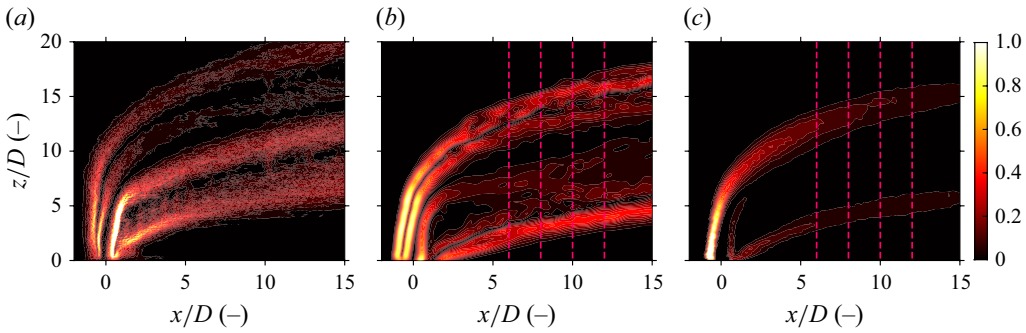


Figure 12. Comparison of normalised spatial gradient magnitude derived from (a) time-averaged OH-PLIF measurements and (b) computed OH mole fraction. (c) Reaction rate, $\bar{\omega}^*$. These quantities are normalised using their respective global maximum.

near-field region, $s/D < 25$, are attributed to the increased jet surface area resulting from circumferential stretching and wrinkling during the CVP formation, as discussed in § 3.1.3. In the far-field region, K_e values for both free jets and JICF converge, reflecting the similarity in the dominant entrainment mechanism. Furthermore, the collapse of K_e across different pressures suggests that while the absolute entrainment rate increases with pressure, the overall mixing pattern remains unaltered when R , S and J are kept constant. It is worth noting that among these parameters, only \dot{m}_j varies across the four cases, further reinforcing this conclusion.

3.2. Reacting jet in cross-flow

3.2.1. Validation

Following ignition, jet and cross-flow fluids react in regions having flammable mixtures. These flame (or reacting) regions are identified in experiments using planar laser-induced fluorescence (PLIF) of hydroxyl (OH) radicals (Hartung *et al.* 2008; Boyette *et al.* 2019; Angelilli *et al.* 2021). Hydroxyl radicals are present in both the flame and burnt products, but at differing levels. Hence, the flame regions can be qualitatively demarcated through the spatial gradient of OH fluorescence (Hartung *et al.* 2008). The magnitude of the spatial gradients, calculated from the time-averaged OH-PLIF and OH mole fractions (X_{OH}) from the LES, are compared in figures 12(a) and 12(b). The general features, spatial extent and the flame locations of both the windward and leeward flame branches from the LES agree well with experimental observations of Boxx *et al.* (2022). In addition, the contours of the time-averaged reaction rate shown in figure 12(c) also compare well with the spatial gradient of OH, suggesting that the flame regions are captured well in the simulations. Notably, some discrepancies are observed on the jet's leeward side, where OH radicals persist in the burnt products despite negligible local reaction rates. This is also verified using instantaneous images from diagnostics and LES, but not shown here. These comparisons remain qualitative, as direct quantitative evaluation of flame-related properties such as temperature or scalar concentration is not possible due to the lack of corresponding experimental data. However, PIV measurement for the reacting flows at the 7 bar case, P7, allows for a quantitative evaluation as it reflects the effect of heat release on the local flow dynamics.

The computed axial and cross-stream velocity statistics are compared with their respective measurements in figure 13 for the case P7. A very good agreement is observed for both mean and r.m.s. values. However, some disagreements are observed for the r.m.s.

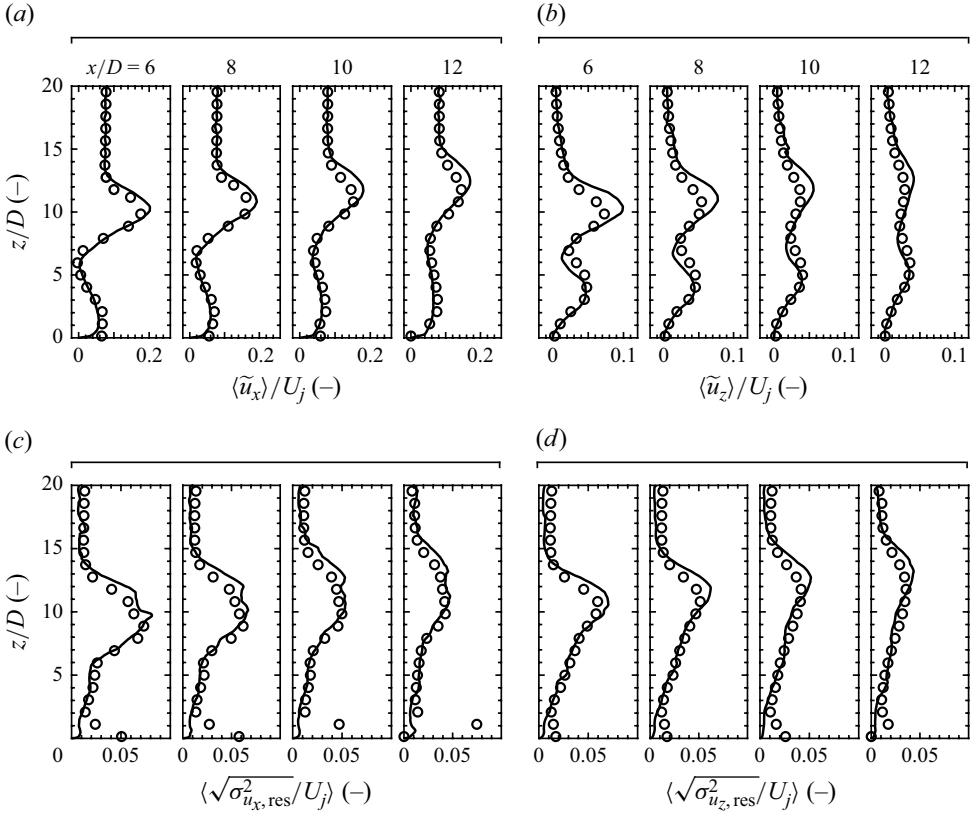


Figure 13. Comparisons of measured (\circ) and computed (—) (a) mean axial and (b) z cross-stream velocities and (c and d) their respective r.m.s values. The cross-stream variations are shown for four axial locations of the case P7. The values are normalised using $U_j = 135 \text{ m s}^{-1}$.

in the near-wall region, $z/D < 2$, which is because the laser reflection from the bottom wall can yield spurious behaviour for second-order statistics. Also, the wall boundary layers are not resolved but modelled in the LES, as noted in § 2.3. For these reasons, one must be careful while comparing the measured and computed near-wall statistics. Furthermore, the average numerical grid size in the mixing region is approximately $0.15\text{--}0.4 \text{ mm}$. This implies turbulent structures of size larger than $9.76\delta_{th}$ and their influences on the flame are resolved in the LES of P7 case. The multi-scale analysis of Doan, Swaminathan & Chakraborty (2017) suggested that eddies of size $2 \leq \delta_{th} \leq 5$ contribute predominantly to the flame straining. These eddies are subgrid scales for the conditions of P7, and hence, one would expect these eddies to influence the reaction rate through flame straining. However, these subgrid eddies have a small amount of kinetic energy associated with them since more than 90 % of the kinetic energy is resolved by the grid (see figure 3). Hence, the flame straining caused by these subgrid scale structures is insignificant compared with that of the resolved scales. Thus, the combustion closure based on the unstrained flamelets model, described in § 2.2, is good for the flow, thermochemical and elevated pressure conditions considered for this study. Furthermore, the good agreement observed for the measured and computed r.m.s. values suggest that the inlet turbulence conditions and the method used to generate it (see § 2.3) mimic the experimental situations well.

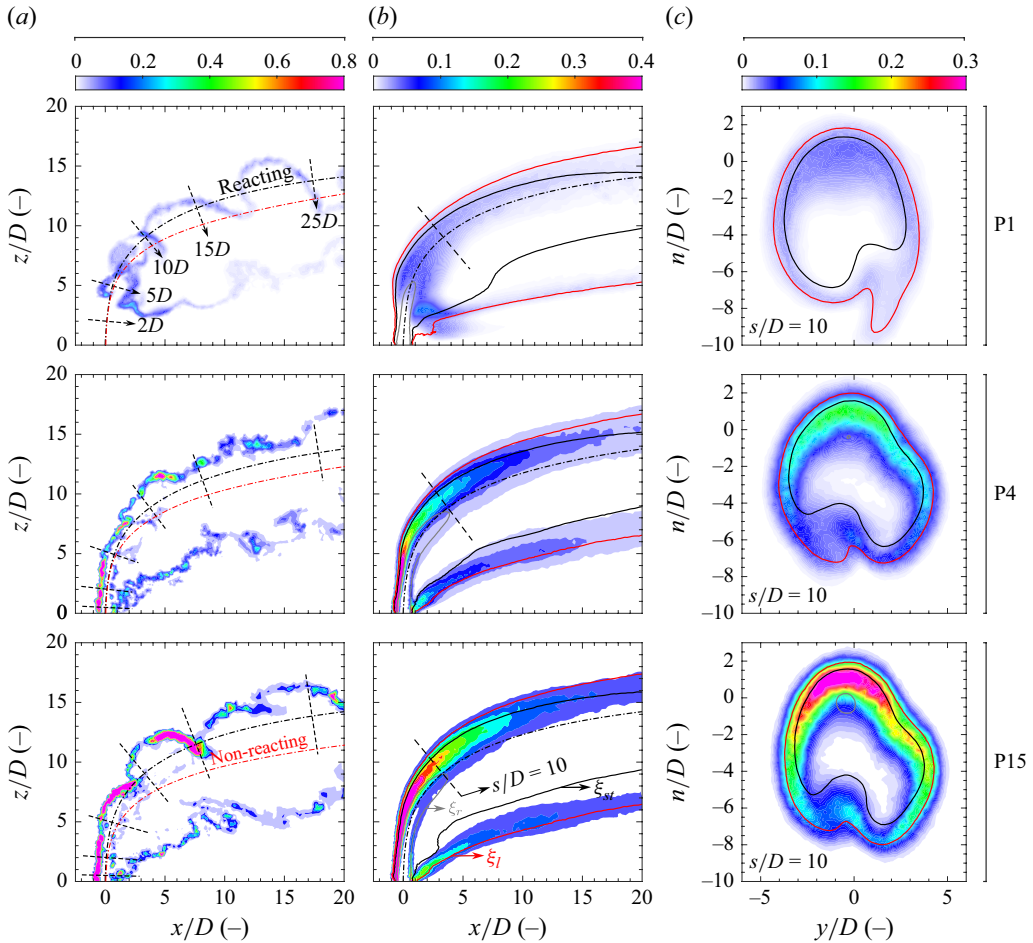


Figure 14. (a) Spatial distribution of \hat{q} in the $y=0$ plane for the cases P1, P4 and P15. (b,c) Corresponding time-averaged variations in the $x-z$ and $y-n$ planes. The locations of the $y-n$ planes are marked in panel (b). The iso-lines of $\langle \tilde{\xi} \rangle = \xi_l$, $\langle \tilde{\xi} \rangle = \xi_r$ and $\langle \tilde{\xi} \rangle = \xi_{st}$ are also shown in panels (b) and (c). The jet trajectories for reacting and non-reacting flows are shown in panel (a) along with various s/D locations used for later analysis.

3.2.2. Spatial distribution of heat release rate

Typical spatial variation of $\hat{q} = \bar{q}/\dot{q}_{P1,max}$, where \bar{q} is the filtered volumetric heat release rate and $\dot{q}_{P1,max}$ is the maximum volumetric heat release rate in a freely propagating stoichiometric (H_2+He)–air laminar flame at atmospheric pressure, are shown in figure 14(a) for the cases P1, P4 and P15. These variations are shown in the $y=0$ plane at $t=6\tau_f$ from ignition. Also, the jet trajectories of corresponding non-reacting and reacting flows are shown for comparison along with a few s/D locations used for further analyses. The contours of \hat{q} show that the predominant heat release is in the shear layers for all the cases. Although the flames are lifted on both the windward and leeward sides on an instantaneous basis they have merged together at $s/D \approx 3.5$ in an averaged sense as suggested by the time-averaged heat release rate distribution shown in figures 14(b) and 14(c) for the atmospheric case. This merging does not occur for the elevated pressure cases, and the spatial distributions of \hat{q} and $\langle \hat{q} \rangle$ are similar for the P4 and P15 cases. The density of the reactants increases with pressure as $\rho_u \propto p_0$, resulting in an increased

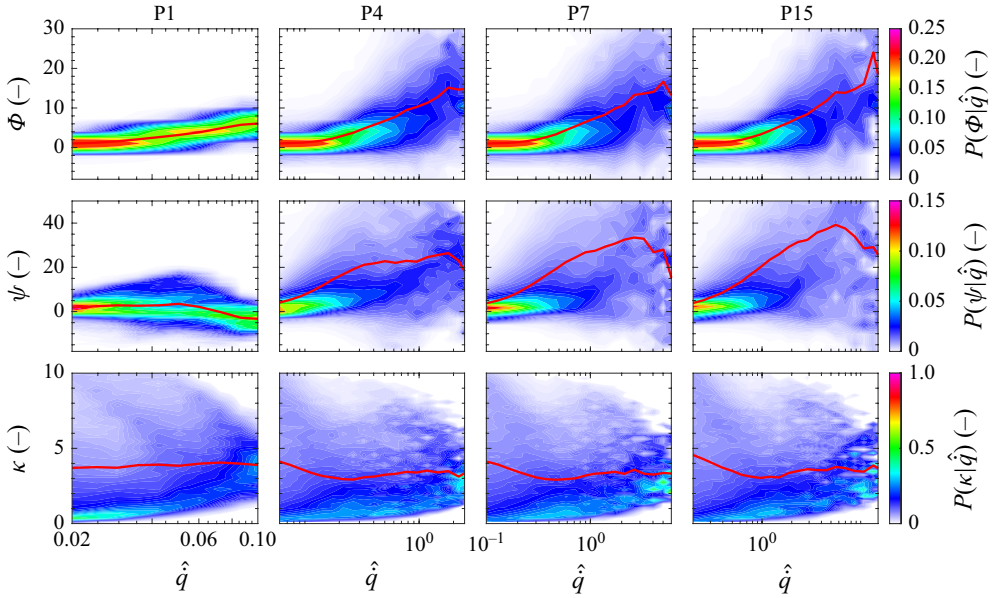


Figure 15. Conditional probability density function (c.p.d.f.s) of Φ , ψ and κ , conditioned on \hat{q} . The respective conditional means are shown by the solid lines (—).

burning flux, $f^0 = \rho_u s_L \propto p_0^{n/2}$, where n is the order of the overall chemical reaction, which is approximately 2 for an H_2 –air flame (Law 2006). Since f^0 represents the eigenvalue of flame propagation, the windward and leeward flame branches move upstream and attach to the jet exit as suggested by the contours of \hat{q} and $\langle \hat{q} \rangle$. The leeward branch is stabilised by the recirculation zone and hence it is quite steady, robust and includes lean mixtures with relatively lower amount of heat release. The distribution of this averaged heat release rate in the jet cross-section is similar to the CVP shape as shown in figure 14(c).

3.2.3. Heat release effects on mixing

It is well established that heat release suppresses entrainment (Hermanson & Dimotakis 1989) by influencing the shear layer roll-up. There are two possible mechanisms behind this influence: the first one being the volumetric expansion or dilatation, which alters the spatial velocity gradients, and the second one being the increase in the total kinematic viscosity of the fluid. The volumetric expansion arises from density changes caused by mixing and chemical reactions. The expansion resulting solely from chemical heat release can be quantified using the pointwise difference in dilatation (also the strain rates and kinematic viscosity discussed later) between the time-averaged reacting and non-reacting flows. This difference is expressed as $\Phi = (\partial \langle \tilde{u}_i \rangle / \partial x_i)_r - (\partial \langle \tilde{u}_i \rangle / \partial x_i)_{nr} / [|E|_{nr}]$, where $|E| = \sqrt{2E_{ij}E_{ij}}$ is the Frobenius norm of the symmetric strain rate tensor E_{ij} . The subscripts ‘ r ’ and ‘ nr ’ denote the reacting and non-reacting conditions, respectively, and the operator $[]$ represents the volume-weighted averaging. The top row of figure 15 shows the conditional probability density function (c.p.d.f.) of Φ , conditioned on the normalised heat release rate \hat{q} . The c.p.d.f.s are computed using 60 bins in each sample space, with data sampled from the reacting regions of the flow, which is defined by $\hat{q} > 0.001 \times [\hat{q}]$. Due to its wide spatial extent, low heat release rates exhibit relatively higher probability. The difference in the dilatation increases with \hat{q} , and since the maximum value of \hat{q} rises

with operating pressure p_0 , the maximum Φ also increases accordingly as reflected by the conditional mean profiles. Furthermore, the density difference between the jet and cross-flow fluids yields non-zero dilatation in the mixing layers of non-reacting flow, and this mixing layer shifts spatially because of expansion effects arising from heat release in reacting flows. Hence, Φ can take some small negative values as observed in the top row of figure 15.

The strain rate magnitude $|E|_{nr}$ is used for normalisation because it reflects the local kinematic deformation of the flow, encompassing both volumetric expansion and shear deformations. While the dilatation term $tr(E_{ij})$ accounts for the volumetric expansion, it does not capture changes in shear deformation due to heat release. To assess this, the change in strain rate magnitude, expressed as $\psi = |E|_r - |E|_{nr} / [|E|_{nr}]$, is calculated. The middle row of figure 15 shows the c.p.d.f.s of ψ with respect to \hat{q} . These contours closely resemble those of Φ : probability is concentrated at low \hat{q} , and the conditional mean increases with \hat{q} and p_0 . This trend reflects the intensification of local velocity gradients due to flow acceleration in the reacting shear layer. At very high values of \hat{q} , the conditional mean of ψ decreases due to sparse sampling. It is important to note that combustion slightly increases the jet penetration depth, subtly shifting the shear layer location radially in downstream regions of $s/D \approx 5$. Consequently, in some regions where the shear layer exists under non-reacting conditions, ψ can become negative. This is particularly evident in case P1, where the flame root (and hence high \hat{q}) lies downstream of this region, resulting in negative conditional means of ψ . However, such behaviour is not observed in the higher-pressure cases, where the flame is anchored closer to the jet exit, coinciding with the peak strain rate location in both reacting and non-reacting conditions.

The effect through the change in the local kinematic viscosity ν can be quantified as $\kappa = \nu_r - \nu_{nr} / [\nu_{nr}]$. The bottom row of figure 15 presents the conditional p.d.f. and the corresponding mean of κ . Notably, there could be two distinct values of ν for a given value of \hat{q} , leading to a reverse-C-shaped distribution in the c.p.d.f.s. The p.d.f.s (as it is the sample fraction) for high κ are small because they arise from locally reacting (in a mean sense) mixture, which typically occupy a small region. While the time scale of chemical kinetics decreases with increasing \hat{q} , the burnt product temperature remains unaltered. Consequently, following Sutherland's law, the normalised change in ν remains constant with respect to \hat{q} and p_0 . Comparing the conditional mean of Φ , ψ and κ reveals that the heat release affects both the local flow dynamics (via strain rate and dilatation) and the thermochemical properties (via viscosity) equally at atmospheric pressure conditions. However, with increasing pressure, the influences on flow dynamics become significantly more pronounced, whereas the effect on viscosity remains essentially constant. At 15 bar, the change in strain rate and dilatation are nearly an order of magnitude larger than the changes in viscosity. These combustion-induced changes in flow dynamics and properties alter the behaviour of the shear layer by locally laminarising the flow, thereby reducing mixing and increasing jet penetration depth (Hasselbrink & Mungal 2001). Furthermore, the periodic roll-up of shear layer vortices is suppressed (Nair *et al.* 2019; Saini *et al.* 2021; Sayadi & Schmid 2021). Since the viscosity-related changes remain insensitive to pressure, it becomes essential to investigate how the substantially large changes in flow dynamics at high pressures govern mixing in the reacting JICF configuration.

The variations of $\langle \xi \rangle$ with s/D for the four reacting conditions are shown in figure 16(a) along with the non-reacting case of P1 for comparison. The flame is lifted in the P1 case and hence the near-field ($s/D \leq 3.8$) mixing is identical for the non-reacting and reacting conditions as seen in the figure. Hence, the jet trajectory is also not disturbed by the heat release as seen in figure 14. The heat release in the subsequent downstream region

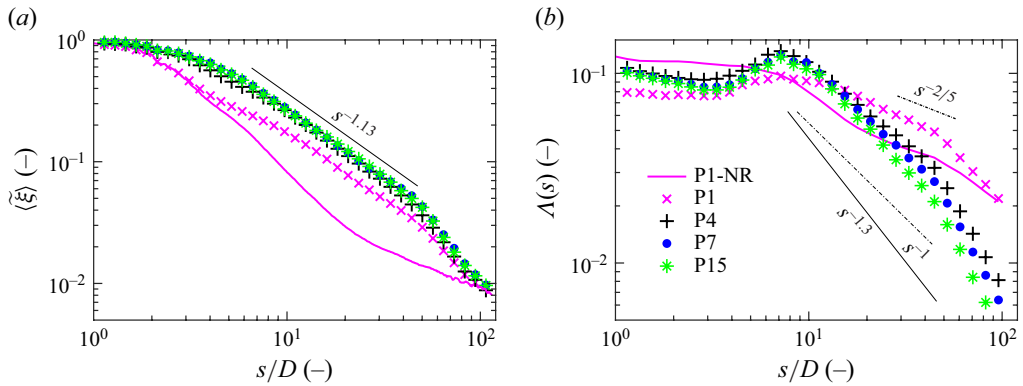


Figure 16. Variation of (a) $\langle \tilde{\xi} \rangle$ and (b) Λ with s/D under reacting conditions.

influences the entrainment, leading to a drop in the decay rate as seen in figure 16(a) and this continues until $s/D \approx 10$. The $\langle \tilde{\xi} \rangle$ varies as $s^{-0.8}$ for $3.5 < s/D < 10$ and it changes to $s^{-1.13}$ for $s/D > 10$. Since the flame is attached to the jet exit, the exponent of -1.13 is also observed for the elevated pressures from $s/D \approx 2.5$. Except for this change, there is no influence of pressure on the mixing as observed for the non-reacting flows in § 3.1.3. This implies that the substantial changes observed in the flow dynamics does not alter the mixing characteristics unduly.

The variation of Λ along the jet centreline is shown in figure 16(b) for all cases. This variation for the non-reacting case of P1 is also shown for comparison. Under the reacting conditions, the local mixture is distributed towards the leeward side due to stirring and mixing supported by the recirculation zone. This results in a relatively lower segregation level in the near-nozzle region ($s/D < 3$) compared with the non-reacting counterpart. As the mixing progresses, the mixture fraction variance and the segregation level decrease with increasing s . As shown in figure 16(a), the mean mixture fraction is higher than its non-reacting counterpart at a given s/D location within the reacting region. This is because the local heat release rate suppresses the entrainment, which preserves scalar segregation. While the variance, σ_{ξ}^2 , and $\langle \tilde{\xi} \rangle$ decrease due to molecular diffusion, Λ increases within the flame region and attains a peak at $s/D \approx 7$, coinciding with the local maximum heat release rate. This suggests that combustion locally suppresses turbulent stirring, lowering $\tilde{\xi}(1 - \tilde{\xi})$. Beyond this point, the heat release rate decreases, allowing further mixing to occur, which lowers the segregation level. For the P4, P7 and P15 cases, the predominant reaction occurs in the windward near-nozzle region and gradually decreases downstream (see figure 14). The suppression of air entrainment by the reaction leads to a relatively higher $\langle \tilde{\xi} \rangle$ in this region, as seen in figure 16(a). Consequently, g_{ξ} and Λ are large for $3 < s/D < 7$. The mixing progresses further as the heat release rate decreases in the downstream region leading to a drop in Λ . Notably, in the low heat release rate region ($s/D \gtrsim 20$), the decay of Λ follows the same scaling as in the corresponding non-reacting case. This indicates that combustion primarily influences the near-field by suppressing shear-driven turbulence, but has a diminishing impact on mixing further downstream.

3.2.4. Combustion modes

Generally, the mixing and combustion have mutual influence in partially premixed combustion, which is the case for the JICF investigated here. Hence, the combustion occurs over a wide range of mixture fractions, covering from lean to rich flammability

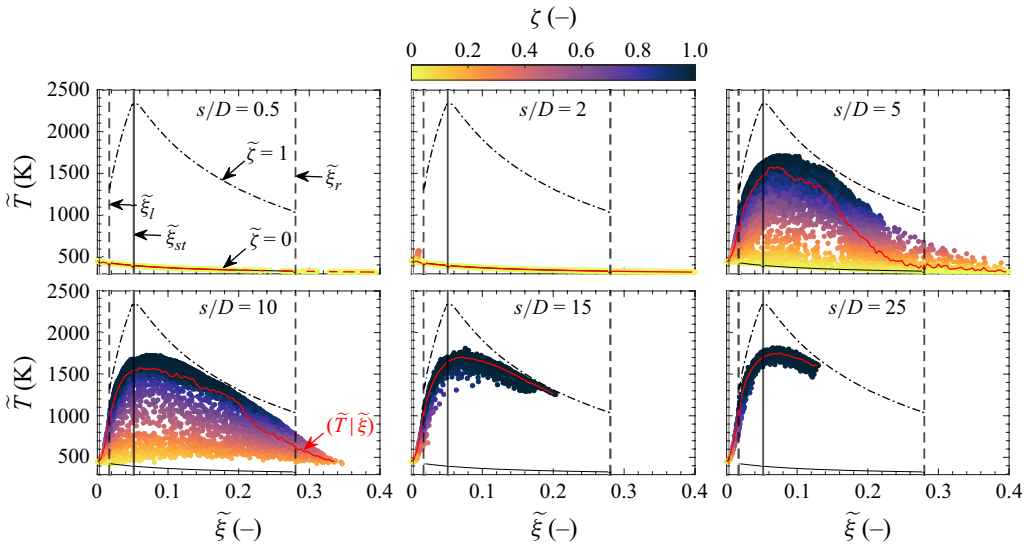


Figure 17. Typical variation of temperature in the mixture fraction space at $t = 6\tau_f$ in the case P1. The conditionally averaged temperature is shown using the red line. The mixing and fully reacting limits are shown using the dash-dotted line. The colour denotes the progress variable.

limits. Also, the range of mixture fraction values over which combustion occurs varies along the jet centreline as discussed in § 3.2.3. To illustrate this further, the temperature variation with the mixture fraction is shown in figure 17 for the case P1. The data collected from a small y - n slices with approximately 1 mm thickness centred around the s/D locations noted in the figure (also marked in figure 14a) are used for the scatter plot. The fully burnt and unburnt limits are also marked using $\zeta = 1$ and 0, respectively. Also, the temporal change of the variations shown in figure 17 is negligible for the data collection period.

The temperature follows the mixing line, $\zeta = 0$, in figure 17 for $s/D = 0.5$ since no combustion occurs in the near-nozzle region. There are some preheated mixtures having $\xi < \xi_l$ for $s/D = 2$ location, which results from the mixing of burnt gases from the leeward side behind the PCR with unburnt gases from the corresponding windward side (see figure 14b). The combustion in $2 \leq s/D \leq 5$ occurs in mixtures with $\xi_{st} < \xi < \xi_r$, as seen in figure 14. The windward and leeward shear layers merge at $s/D = 5$ accelerating the break-up of the jet and its mixing with the cross-flow fluid as observed in figure 16(a). As a result, the $\langle \xi \rangle = \xi_r$ iso-contour does not extend beyond $s/D = 5$, see figure 14. Hence, the combustion here occurs over the entire flammable range as shown in figure 17 with some non-reacting mixtures, signified by the data points on the $\zeta = 0$ line. This preheated mixture and those created through the mixing of burnt and unburnt mixtures react at further downstream locations which is signified by the shift of the data from the $\zeta = 0$ line at the $s/D = 10$ location. A substantial amount of fuel is consumed before s/D of 25 and hence the samples are within $\xi = 0$ to 0.14.

The results for the P15 case are presented in figure 18 for comparison. The increased pressure shifts the flame stabilisation point closer to the jet exit. Consequently, both preheated and near fully burnt mixtures are observed for the $s/D = 0.5$ location, where fuel-rich combustion predominantly occurs on the windward side while fuel-lean combustion is on the leeward side as evident in figure 14. The dominant reactions occur in highly reactive mixture fractions with low ignition delay times. These reactions preheat the

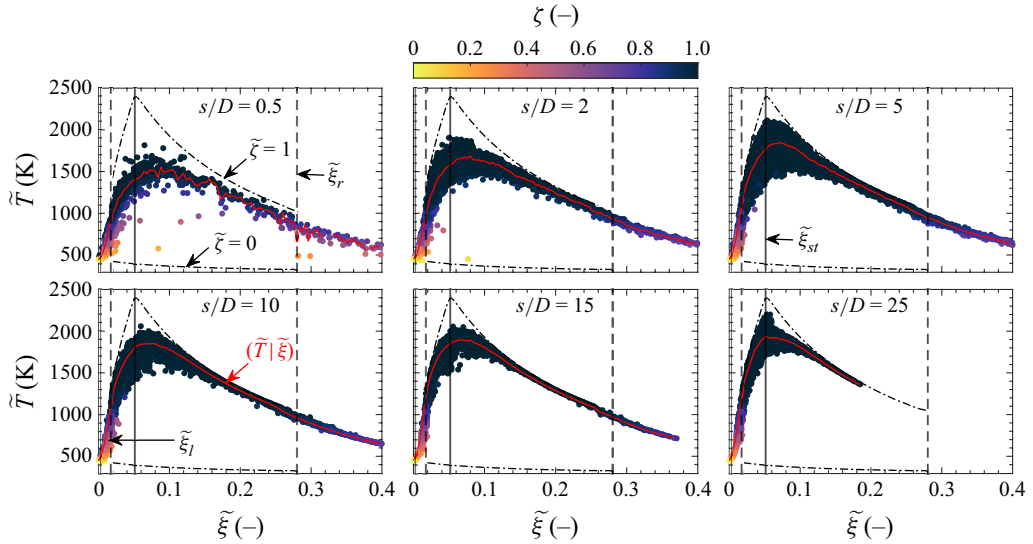


Figure 18. Temperature variation with the mixture fraction is shown for the case P15 at $t = 6\tau_f$ and the colour denotes the reaction progress variable. The conditionally averaged temperature is shown using a red line. The mixing and fully burnt reacting limits are shown using the dash-dotted lines.

downstream mixture triggering an ignition cascade that leads to subsequent combustion of stoichiometric and richer mixtures. Therefore, the combustion at $s/D = 2, 5$ and 10 occurs across the entire flammable range. Similar to the case P1, combustion at $s/D = 15$ and 25 occurs under fuel-lean conditions. This narrows the spatial distribution of the reacting region and increases the progress variable gradient. Hence, significant variation in ζ is not observed in P15. Moreover, the heat release rate suppresses the formation of coherent structures along the shear layer. Therefore, the reacting region present closer to the jet exit in P15 reduces the rate at which the jet breaks up, which also contributes to the lack of preheated mixtures in the P15 case.

The previous discussion highlights the pressure effect in the mixture fraction range with combustion in the JICF. However, it does not elucidate the combustion modes. Both premixed and non-premixed modes are present in partially premixed combustion. Therefore, the transport equation of the reaction progress variable has two source terms as written in (2.5). The relative contributions of these two modes can be investigated using a joint p.d.f. of η and γ , where γ is the sample space variable for $\Omega = \bar{\omega}_{np}/\bar{\omega}_{fp}$ (Massey *et al.* 2023a). It is important to note that a flame is likely to burn in a premixed mode if the reactant mixture is within the flammability limit and hence the significant burning along the stoichiometric iso-contours, observed in figure 14, is just not a characteristic of non-premixed mode alone as it includes contributions of stoichiometric premixed combustion as well. However, $\bar{\omega}_{np}$ denotes non-premixed contribution and it comes from the neighbourhood of ξ_{st} since $d^2Y_{H_2O}^b/d\eta^2$ is non-zero only in that region. The variation of $d^2Y_{H_2O}^b/d\eta^2$ in the mixture fraction space has been discussed by Ruan, Swaminathan & Darbyshire (2014) for an H_2 –air mixture under atmospheric pressure and it does not differ significantly for elevated pressures. Also, Ω is 0 in the fully premixed limit and $-\infty$ in the non-premixed limit.

The fractional contribution of the non-premixed mode from the lean, rich and the stoichiometric mixtures can be obtained by taking appropriate moments of the joint p.d.f. as

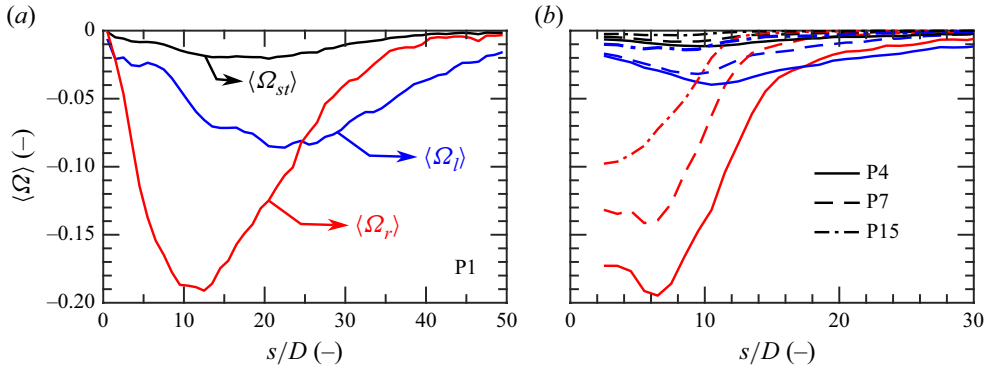


Figure 19. Variations of the time-averaged fractional contribution from the non-premixed mode in the lean, $\langle \Omega_l \rangle$, stoichiometric, $\langle \Omega_{st} \rangle$, and rich, $\langle \Omega_r \rangle$, mixture fractions. The variation at atmospheric pressure is shown in panel (a) while that for 4, 7 and 15 bars are shown in panel (b).

$$\begin{aligned} \langle \Omega \rangle = & \underbrace{\int_{\tilde{\xi}_l}^{\tilde{\xi}_{st}-\Delta\tilde{\xi}} \int_{-\infty}^0 \gamma P(\eta, \gamma) d\gamma d\eta}_{\langle \Omega_l \rangle} + \underbrace{\int_{\tilde{\xi}_{st}-\Delta\tilde{\xi}}^{\tilde{\xi}_{st}+\Delta\tilde{\xi}} \int_{-\infty}^0 \gamma P(\eta, \gamma) d\gamma d\eta}_{\langle \Omega_{st} \rangle} \\ & + \underbrace{\int_{\tilde{\xi}_{st}+\Delta\tilde{\xi}}^{\tilde{\xi}_r} \int_{-\infty}^0 \gamma P(\eta, \gamma) d\gamma d\eta}_{\langle \Omega_r \rangle}. \end{aligned} \quad (3.4)$$

Here, $\Delta\tilde{\xi} \approx 0.0026$, which is approximately 5 % of $\tilde{\xi}_{st}$. The data used for constructing the joint p.d.f. are obtained over the final $1\tau_f$ period of the simulations. The moments in (3.4) are calculated using the data from different y - n slices to show their variations along s/D , as depicted in figure 19.

The fractional contribution magnitude of the non-premixed mode is below 0.2 irrespective of the mixture fraction values for the range of pressures considered here. This suggests that the combustion is predominantly in premixed mode. The mixing among the fuel and entrained air on the windward side and products from the leeward side can alter the contribution of the non-premixed mode. Since the flame is lifted in the P1 case, the reaction rates are zero in the near field and start to increase specifically on the rich side until $s/D \approx 11$, also see figure 14(b). Since a significant amount of fuel is mixed well and also burnt in region $s/D \lesssim 11$, the combustion shifts to fuel-lean condition in the subsequent downstream locations, leading to their dominant contributions to $\langle \Omega \rangle$, as seen in figure 19. The flame moves upstream and is attached to the nozzle as the pressure is increased and hence non-zero contributions from the rich, lean and stoichiometric mixtures are observed from the jet exit. As seen in figure 14, the predominant heat release is along the shear layers even for the elevated pressures and hence the major contribution to $\langle \Omega \rangle$ comes from the fuel-rich side. Also, this non-premixed contribution is relatively larger than $\langle \Omega_l \rangle$ and $\langle \Omega_{st} \rangle$ for the elevated pressures because of the attached flames. However, the fractions of non-premixed contributions decreases substantially when the pressure is changed from 4 to 15 bar suggesting that the premixed combustion mode dominates both locally and in an averaged sense despite the fact that the fuel and air are injected through separate streams.

4. Conclusion

This study investigates pressure effects on the mixing characteristics in JICF for both reacting and non-reacting conditions using LES. A hydrogen jet with 30 % helium by volume is injected normal to cross-flowing air. The simulations considered 1, 4, 7 and 15 bar while keeping the jet to cross-flow velocity, density and momentum flux ratios constant. The LES statistics for the 7 bar non-reacting case agreed well with measurements. Mixing characteristics are studied using the variations of mixture fraction and unmixedness, Λ , along the jet centreline, s . The averaged mixture fraction, $\langle \tilde{\xi} \rangle$, decays as $s^{-1.3}$ in the near-field and $s^{-2/3}$ in the far-field regions, which are faster compared with s^{-1} for a free jet. The variations of both $\langle \tilde{\xi} \rangle$ and Λ along the jet centreline reveals that the mixing characteristics are not sensitive to the pressure. For a given momentum flux ratio, increasing the pressure increases the jet and cross-flow mass flow rates and hence the absolute entrainment rate increases without altering the overall mixing pattern under non-reacting conditions.

The spatial distribution of heat release rate and velocity statistics computed for the 7 bar case agreed well with OH-PLIF imaging and PIV measurements (Boxx *et al.* 2022). The combustion in the mid-streamwise plane occurs in three distinct branches: two along the jet shear layer and one along the locus of the counter-rotating vortex pair lobes. The leeward branch is stabilised by the recirculation zone with hot products present there for all the pressures, whereas the windward branch transitioned from a lifted flame for 1 bar to attached flame for elevated pressures. This change is because of the increased burning flux with pressure. The comparisons between reacting and non-reacting results show that combustion suppresses mixing specifically at elevated pressures since the attached windward flame reduces the entrainment of cross-flowing air into the fuel jet. This changes the decay scaling to $s^{-1.13}$ from $s^{-1.3}$ for non-reacting conditions as noted previously. However, the metrics related to scalar mixing remained almost constant for the 4, 7 and 15 bar cases, suggesting that flame stabilisation location is the key factor dictating the local mixing characteristics in JICF. The metrics are unaffected by pressure once the flame is attached to the jet exit.

This study further demonstrates that combustion modes change along the jet trajectory with pressure. As noted earlier, the combustion occurs along three branches – the windward and leeward shear layer branches, and one along the lobes of the counter-rotating vortex pair. The fuel-rich windward branch becomes more pronounced at the elevated pressures. As the mixing proceeds along the jet trajectory, the combustion moves to fuel-lean conditions which is also the case for the flame branch along the lobes of the counter-rotating vortex pair. Furthermore, the contribution of non-premixed mode to the overall partially premixed combustion is observed to be substantially lower than premixed mode for all the pressures and this contribution decreases further with an increase in pressure. Hence, this study suggests that the premixed mode is the predominant mode of heat release in the partially premixed combustion in JICF despite the air and fuel being fed through separate streams.

Acknowledgements. This work used the ARCHER2 UK National Supercomputing Service (<http://www.archer2.ac.uk>) and the EPSRC Tier2 National HPC service, CSD3 (<http://www.hpc.cam.ac.uk/high-performance-computing>).

Funding. This work received funding from Mitsubishi Heavy Industries, Ltd., Takasago, Japan and EPSRC through ARCHER2 Pioneer Project, e808 is acknowledged for the financial and computational allocation.

Declaration of interests. The authors report no conflict of interest.

Data availability statement. The data can be made available to interested readers by contacting the corresponding author.

Author contributions. A. B. Murugavel: Writing original draft, reviewing & editing, Visualisation, Validation, Formal analysis, Conceptualisation. J. C. Massey: reviewing & editing, Software, analysis. N. Swaminathan: reviewing & editing, Supervision, Resources, Project administration, Funding acquisition, Conceptualisation.

REFERENCES

- ANGELILLI, L., CIOTTOLI, P.P., GUIBERTI, T.F., GALASSI, R.M., PÉREZ, F.E.H., BOYETTE, W.R., MAGNOTTI, G., ROBERTS, W.L., VALORANI, M. & IM, H.G. 2021 A method to convert stand-alone OH fluorescence images into OH mole fraction. *Proc. Combust. Inst.* **38** (1), 1771–1778.
- BILGER, R.W. 1989 The structure of turbulent nonpremixed flames. *Symp. (Intl) Combust.* **22** (1), 475–488.
- BOXX, I., PAREJA, R.J. & SAINI, P. 2022 An experimental study of natural gas jet-flames in crossflow with high hydrogen admixture at elevated pressure conditions. In *20th International Symposium on Applications of Laser and Imaging Techniques to Fluid Mechanics*. Available at: <https://doi.org/10.55037/ixlaser.20th.199>.
- BOYETTE, W.R., GUIBERTI, T.F., MAGNOTTI, G. & ROBERTS, W.L. 2019 Structure of turbulent nonpremixed syngas flames at high pressure. *Proc. Combust. Inst.* **37** (2), 2207–2214.
- BROADWELL, J.E. & BREIDENTHAL, R.E. 1984 Structure and mixing of a transverse jet in incompressible flow. *J. Fluid Mech.* **148**, 405–412.
- CHEN, Z., RUAN, S. & SWAMINATHAN, N. 2017 Large Eddy Simulation of flame edge evolution in a spark-ignited methane–air jet. *Proc. Combust. Inst.* **36** (2), 1645–1652.
- CHEN, Z.X., LANGELLA, I., BARLOW, R.S. & SWAMINATHAN, N. 2020 Prediction of local extinctions in piloted jet flames with inhomogeneous inlets using unstrained flamelets. *Combust. Flame* **212**, 415–432.
- CHEN, Z.X., LANGELLA, I., SWAMINATHAN, N., STÖHR, M., MEIER, W. & KOLLA, H. 2019 Large Eddy Simulation of a dual swirl gas turbine combustor: flame/flow structures and stabilisation under thermoacoustically stable and unstable conditions. *Combust. Flame* **203**, 279–300.
- COELHO, S.L.V. & HUNT, J.C.R. 1989 The dynamics of the near field of strong jets in crossflows. *J. Fluid Mech.* **200**, 95–120.
- DIMOTAKIS, P.E. & MILLER, P.L. 1990 Some consequences of the boundedness of scalar fluctuations. *Phys. Fluids A: Fluid Dyn.* **2** (11), 1919–1920.
- DOAN, N.A.K., SWAMINATHAN, N. & CHAKRABORTY, N. 2017 Multiscale analysis of turbulence-flame interaction in premixed flames. *Proc. Combust. Inst.* **36** (2), 1929–1935.
- DUNSTAN, T.D., MINAMOTO, Y., CHAKRABORTY, N. & SWAMINATHAN, N. 2013 Scalar dissipation rate modelling for Large Eddy Simulation of turbulent premixed flames. *Proc. Combust. Inst.* **34** (1), 1193–1201.
- VON ELBE G. & LEWIS B. 1942 Mechanism of the thermal reaction between hydrogen and oxygen. *J. Chem. Phys.* **10** (6), 366–393.
- FEARN, R. & WESTON, R.P. 1974 Vorticity associated with a jet in a cross flow. *AIAA J.* **12** (12), 1666–1671.
- FRIC, T.F. & ROSHKO, A. 1994 Vortical structure in the wake of a transverse jet. *J. Fluid Mech.* **279**, 1–47.
- GETSINGER, D.R., GEVORKYAN, L., SMITH, O.I. & KARAGOZIAN, A.R. 2014 Structural and stability characteristics of jets in crossflow. *J. Fluid Mech.* **760**, 342–367.
- GOODWIN, D.G., MOFFAT, H.K. & SPETH, R.L. 2017 Cantera: an object-oriented software toolkit for chemical kinetics, thermodynamics, and transport processes. Available at: <http://www.cantera.org> (Accessed: 10 Jan 2022).
- HARTUNG, G., HULT, J., KAMINSKI, C.F., ROGERSON, J.W. & SWAMINATHAN, N. 2008 Effect of heat release on turbulence and scalar-turbulence interaction in premixed combustion. *Phys. Fluids* **20** (3), 035110.
- HASSELBRINK, E.F. & MUNGAL, M.G. 2001 Transverse jets and jet flames. Part 1. Scaling laws for strong transverse jets. *J. Fluid Mech.* **443**, 1–25.
- HERMANSON, J.C. & DIMOTAKIS, P.E. 1989 Effects of heat release in a turbulent, reacting shear layer. *J. Fluid Mech.* **199**, 333–375.
- HILL, B.J. 1972 Measurement of local entrainment rate in the initial region of axisymmetric turbulent air jets. *J. Fluid Mech.* **51** (4), 773–779.
- JANICKA, J. & PETERS, N. 1982 Prediction of turbulent jet diffusion flame lift-off using a pdf transport equation. *Symp. (Intl) Combust.* **19**, 367–374.
- JARRIN, N., BENHAMADOU, S., LAURENCE, D. & PROSSER, R. 2006 A synthetic-eddy-method for generating inflow conditions for large-eddy simulations. *Intl J. Heat Fluid Flow* **27** (4), 585–593.
- KAMOTANI, Y. & GREBER, I. 1972 Experiments on a turbulent jet in a cross flow. *AIAA J.* **10** (11), 1425–1429.
- KANKANWADI, K.S. & BUXTON, O.R.H. 2023 Influence of freestream turbulence on the near-field growth of a turbulent cylinder wake: turbulent entrainment and wake meandering. *Phys. Rev. Fluids* **8** (3), 034603.
- KARAGOZIAN, A.R. 2010 Transverse jets and their control. *Prog. Energy Combust. Sci.* **36** (5), 531–553.

- KELSO, R.M. & SMITS, A.J. 1995 Horseshoe vortex systems resulting from the interaction between a laminar boundary layer and a transverse jet. *Phys. Fluids* **7** (1), 153–158.
- KOLLA, H., ROGERSON, J.W., CHAKRABORTY, N. & SWAMINATHAN, N. 2009 Scalar dissipation rate modeling and its validation. *Combust. Sci. Technol.* **181** (3), 518–535.
- KUZO, D.M. 1996 *An Experimental Study of the Turbulent Transverse Jet*. California Institute of Technology.
- LANGELLA, I. & SWAMINATHAN, N. 2016 Unstrained and strained flamelets for LES of premixed combustion. *Combust. Theory Model.* **20** (3), 410–440.
- LANGELLA, I., SWAMINATHAN, N. & PITZ, R.W. 2016a Application of unstrained flamelet SGS closure for multi-regime premixed combustion. *Combust. Flame* **173**, 161–178.
- LANGELLA, I., SWAMINATHAN, N., WILLIAMS, F.A. & FURUKAWA, J. 2016b Large-Eddy Simulation of premixed combustion in the corrugated-flamelet regime. *Combust. Sci. Technol.* **188** (9), 1565–1591.
- LAW, C.K. 2006 *Combustion Physics*. Cambridge University Press.
- LIEUWEN, T., McDONELL, V., PETERSEN, E. & SANTAVICCA, D. 2006 Fuel flexibility influences on premixed combustor blowout, flashback, autoignition and instability. *Turbo Expo: Power Land Sea Air* **42363**, 601–615.
- LILLY, D.K. 1992 A proposed modification of the Germano subgrid-scale closure method. *Phys. Fluids A* **4** (3), 633–635.
- MAHESH, K. 2013 The interaction of jets with crossflow. *Ann. Rev. Fluid Mech.* **45** (1), 379–407.
- MARGASON, R.J. 1993 Fifty years of jet in cross flow research. In *Proceedings of the AGARD Symposium on Computational and Experimental Assessment of Jets in Cross Flow*, AGARD CP-534, pp.1–141.
- MASSEY, J.C., LANGELLA, I. & SWAMINATHAN, N. 2018 Large Eddy Simulation of a bluff body stabilised premixed flame using flamelets. *Flow Turbul. Combust.* **101** (4), 973–992.
- MASSEY, J.C., LI, Z., CHEN, Z.X., TANAKA, Y. & SWAMINATHAN, N. 2023a Large eddy simulation of multi-regime combustion with a two-progress variable approach for carbon monoxide. *Proc. Combust. Inst.* **39** (2), 2117–2127.
- MASSEY, J.C., TANAKA, Y. & SWAMINATHAN, N. 2023b Application of a two-progress variable model for carbon monoxide emissions from turbulent premixed and partially premixed enclosed flames. *Combust. Flame* **258**, 113047.
- METHLING, T., BRAUN-UNKHOFF, M. & RIEDEL, U. 2020 An optimised chemical kinetic model for the combustion of fuel mixtures of syngas and natural gas. *Fuel* **262**, 116611.
- MOUSSA, Z.M., TRISCHKA, J.W. & ESKINAZI, S. 1977 The near field in the mixing of a round jet with a cross-stream. *J. Fluid Mech.* **80** (1), 49–80.
- MULDOON, F. & ACHARYA, S. 2010 Direct numerical simulation of pulsed jets-in-crossflow. *Comput. Fluids* **39** (10), 1745–1773.
- MUPPIDI, S. & MAHESH, K. 2005 Study of trajectories of jets in crossflow using direct numerical simulations. *J. Fluid Mech.* **530**, 81–100.
- MURUGAVEL, A.B., MASSEY, J.C., TANAKA, Y. & SWAMINATHAN, N. 2024 The effect of methane addition on reacting hydrogen jets in crossflow. *Intl J. Hydrogen Energy* **80**, 57–67.
- NAIR, V., WILDE, B., EMERSON, B. & LIEUWEN, T. 2019 Shear layer dynamics in a reacting jet in crossflow. *Proc. Combust. Inst.* **37** (4), 5173–5180.
- PIERCE, C.D. & MOIN, P. 1998 A dynamic model for subgrid-scale variance and dissipation rate of a conserved scalar. *Phys. Fluids* **10** (12), 3041–3044.
- POPE, S.B. 2000 *Turbulent Flows*. Cambridge University Press.
- RAHMAN, M.M., IBRAHIM, T.K., KADIRGAMA, K., MAMAT, R. & BAKAR, R.A. 2011 Influence of operation conditions and ambient temperature on performance of gas turbine power plant. *Adv. Materials Res.* **189**, 3007–3013.
- RUAN, S., SWAMINATHAN, N., BRAY, K.N.C., MIZOBUCHI, Y. & TAKENO, T. 2012 Scalar and its dissipation in the near field of turbulent lifted jet flame. *Combust. Flame* **159** (2), 591–608.
- RUAN, S., SWAMINATHAN, N. & DARBYSHIRE, O. 2014 Modelling of turbulent lifted jet flames using flamelets: a priori assessment and a posteriori validation. *Combust. Theory Model.* **18** (2), 295–329.
- SAINI, P., CHTEREV, I., PAREJA, J., AIGNER, M. & BOXX, I. 2020 Effect of pressure on hydrogen enriched natural gas jet flames in crossflow. *Flow Turbul. Combust.* **105** (3), 787–806.
- SAINI, P., CHTEREV, I., PAREJA, J., AIGNER, M. & BOXX, I. 2021 Effects of hydrogen-enrichment on flame-holding of natural gas jet flames in crossflow at elevated temperature and pressure. *Flow Turbul. Combust.* **107** (1), 219–243.
- SAYADI, T. & SCHMID, P.J. 2021 Frequency response analysis of a (non-) reactive jet in crossflow. *J. Fluid Mech.* **922**, A15.
- SMITH, S.H. & MUNGAL, M.G. 1998 Mixing, structure and scaling of the jet in crossflow. *J. Fluid Mech.* **357**, 83–122.

- SPALDING, D.B. 1961 A single formula for the law of the wall. *J. Appl. Mech.* **28** (3), 455–458.
- SU, L.K. & MUNGAL, M.G. 2004 Simultaneous measurements of scalar and velocity field evolution in turbulent crossflowing jets. *J. Fluid Mech.* **513**, 1–45.
- WELLER, H.G., TABOR, G., JASAK, H. & FUREBY, C. 1998 A tensorial approach to computational continuum mechanics using object-oriented techniques. *Comput. Phys.* **12** (6), 620–631.
- YORK, W.D., ZIMINSKY, W.S. & YILMAZ, E. 2013 Development and testing of a low NO_x hydrogen combustion system for heavy-duty gas turbines. *J. Engng Gas Turbines Power* **135** (2), 022001.
- YUAN, L.L. & STREET, R.L. 1998 Trajectory and entrainment of a round jet in crossflow. *Phys. Fluids* **10** (9), 2323–2335.